Master Thesis

Studies of the suppressed B meson decays $B^- \to [K^+\pi^-]_D K^-$ and $B^- \to [K^+\pi^-]_D \pi^-$

$$B \qquad\qquad [K^+\pi^-]_D K^- \quad [K^+\pi^-]_D \pi^-$$

Department of Physics, Tohoku University

Horii Yasuyuki

2008

Abstract

We report a study of the suppressed B meson decay $B^- \to [K^+\pi^-]_D K^-$, where $[K^+\pi^-]_D$ indicates that the $K^+\pi^-$ pair originates from D^0 or $\bar{D}^0$. This decay mode plays an important role in the extraction of the CP-violating angle ϕ_3. We use a data sample containing $657 \times 10^6 B\bar{B}$ pairs recorded at the $\Upsilon(4S)$ resonance with the Belle detector at the KEKB asymmetric e^+e^- storage ring. The signal is not statistically significant, and we set a 90% C.L. upper limit of $r_B < 0.19$, where r_B is the magnitude of the ratio of amplitudes $|A(B^- \to \bar{D}^0 K^-)/A(B^- \to D^0 K^-)|$. The ADS fit is also performed, and we set $r_B < 0.09$ at 90% C.L., while the constraint on ϕ_3 is not strong. For the reference decay $B^- \to [K^+\pi^-]_D \pi^-$, we observe a signal with 8.4σ statistical significance, and measure the charge asymmetry $\mathcal{A}_{D\pi}$ to be $-0.023 \pm 0.218 \pm 0.071$, which is consistent with the expectation. Additionally, the ratio $\mathcal{B}(B^- \to D^0 K^-)/\mathcal{B}(B^- \to D^0 \pi^-)$ is measured to be $(6.77 \pm 0.23 \pm 0.30) \times 10^{-2}$.

Acknowledgements

Contribution of the Author

This thesis is based on the contributions of the Belle members in collaboration with author. The experimental apparatus described in chapter 3 is constructed and managed by the Belle collaboration and KEKB accelerator group, and there are only very small contributions by me, such as a measured-beam-energy installation to the software farm. Also, the tool of particle identification, the tool to study the differences of efficiencies of particle identification requirements between in data and in Monte Carlo samples, the tool to constrain a mass or a vertex with varying the tracks, and the tool to suppress continuum backgrounds, which are described in chapter 4, are all developed by several subgroups. For those points, the author has only used the codes with some changes to make them meet the decays analyzed in this thesis. Additionally, many ideas and many basic tools, such as ROOT, in chapter 1, 2, 4, 5 are based on many contributors, while the author is a primary contributor on the analysis upon the tools and has a responsibility on the results.

Contents

Chapter 1

Introduction

Before the development of modern science, the metaphysics[1] known as "natural philosophy" has contained scientific questions. However, the scientific revolution made natural philosophy as empirical and experimental activity unlike the rest of philosophy, and it had begun to be called "science" in order to distinguish it from philosophy. Then, the metaphysics became the philosophical inquiry of a non-empirical character into the nature of existence. Nowadays, the development of philosophy has provided the idea that the science is in fact one of the metaphysics as a non-empirical activity. This concept is based on the standpoint that the science intends to connect the scientific knowledge to the reality of the nature while this connection seems not to be confirmed with empirical or experimental activity since the identification of the truth seems impossible.

However, the resulting knowledge of the science has actually revolutionized our view of the world, and transforming our society. Even if we can't achieve to know the reality of the nature, the development of the science may bring us closer to the truth and may fertilize our lives. Especially the particle physics is a primary avenue of inquiry into the basic working of the nature. The progression of the particle physics may help us to intend to answer to the fundamental questions such as "What is the nature and the life?"

In twentieth century, the Standard Model of particle physics has been developed with the confirmation of many of its aspects [1]. Almost all experimental tests of the three forces and the matters described by the Standard Model have agreed with its predictions. However, the Standard Model does not contain the explanations for the questions such as "Why do the quarks and the leptons of three generations have different masses and do the mixings among the generations make the CP violation?" There are many input parameters in the Yukawa term and is equivalent to many parameters in quark- and lepton-sectors, while the gauge interaction is based on one coupling constant. At this point, it seems natural to consider the Standard Model is not an ultimate theory. Additionally, the Standard Model contains some problems such as the quadratical divergence of the radiative corrections of the Higgs boson mass squared [2], and no explanations of neutrino mass, dark matter [2], and the fourth force gravity.

One of the way to pursue the physics beyond the Standard Model is to develop the

---

[1]Metaphysics is the branch of philosophy, and the name derives from the Greek words metá (meaning "after") and physiká (meaning "physics").

"Flavor physics." The measurements of the many parameters in the quark- and lepton-sectors are needed as the first steps for that approach. In this thesis, we study about a suppressed B meson decay related to the CP-violating angle ϕ_3, which is one of the parameters in the quark-sector in the Standard Model. Also, one of reference decay is analyzed, for which the CP asymmetry is expected to be negligible.

Chapter 2

CKM matrix and CP-violating angle ϕ_3

2.1 CKM matrix

The Cabbibo-Kobayashi-Maskawa (CKM) matrix $\boldsymbol{V}$ [3, 4] is a three-by-three quark mixing matrix,

$$\boldsymbol{V} = \begin{pmatrix} V_{ud} & V_{us} & V_{ub} \\ V_{cd} & V_{cs} & V_{cb} \\ V_{td} & V_{ts} & V_{tb} \end{pmatrix}, \tag{2.1}$$

where the unitarity of $\boldsymbol{V}$ or

$$\sum_j V_{ij} V_{kj}^* = \delta_{ik} \quad (i, j, k = 1, 2, 3) \tag{2.2}$$

is required in the diagonalizations of mass terms of the quarks[1]. Denoting up- and down-type quarks in mass eigenstate basis as

$$U = \begin{pmatrix} u \\ c \\ t \end{pmatrix}, \quad D = \begin{pmatrix} d \\ s \\ b \end{pmatrix}, \tag{2.3}$$

the interactions of quarks and $W^\pm$ bosons can be written with a current Lagrangian [5] of

$$\mathcal{L}_{\text{int,qW}} = -\frac{g}{\sqrt{2}} \Big[\left(\overline{U}_L \gamma^\mu \boldsymbol{V} D_L \right) W_\mu^+ + \left(\overline{D}_L \gamma^\mu \boldsymbol{V}^\dagger U_L \right) W_\mu^- \Big], \tag{2.4}$$

where the subscript L shows the left-handedness.

We then calculate the numbers of degrees of freedom and possible complex phases of $\boldsymbol{V}$. At first, we assume N generations for the quarks. In general, N-by-N complex matrix $\boldsymbol{V}$ has $2N^2$ of degrees of freedom. The unitarity of $\boldsymbol{V}$ reduces N^2 of those, and

---

[1]The mass terms of quarks are based on the Yukawa term with a spontaneous symmetry breaking.

we also have to consider the phases of the quarks. Since the phases of quarks do not have effects on the physics, we can suppress some degrees of freedom using the phase transitions. However, the same phase changes for all quarks do not vary the matrix $\boldsymbol{V}$. So we reject $2N - 1$ at total by phase transitions of quarks. Therefore, we get the number of degrees of freedom as

$$2N^2 - N^2 - (2N - 1) = N^2 - 2N + 1 = (N - 1)^2. \tag{2.5}$$

Possible complex phases in $\boldsymbol{V}$ is then obtained as follows: Considering the case without complex components, the unitary condition of $\boldsymbol{V}$ is equivalent to the orthogonal conditions,

$$\sum_j V_{ij} V_{kj} = \delta_{ik} \quad (i \le k), \tag{2.6}$$

The number of degrees of freedom of real components are then $N^2 - (N + 1)N/2 = N(N - 1)/2$. Finally, the possible complex components are

$$(N - 1)^2 - \frac{N(N - 1)}{2} = \frac{(N - 1)(N - 2)}{2}. \tag{2.7}$$

When $N = 3$, $\boldsymbol{V}$ has at least one complex phase for all phase choices of the quarks, which reveal the CP violation [5].

It is experimentally known that we can parameterize the matrix $\boldsymbol{V}$ as

$$\boldsymbol{V} = \begin{pmatrix} 1 - \frac{1}{2}\lambda^2 & \lambda & A\lambda^3(\rho - i\eta) \\ -\lambda & 1 - \frac{1}{2}\lambda^2 & A\lambda^2 \\ A\lambda^3(1 - \rho - i\eta) & -A\lambda^2 & 1 \end{pmatrix} + \mathcal{O}(\lambda^4), \tag{2.8}$$

which is a power series of λ (~ 0.23) and provided by Wolfenstein [6]. Actually the number of degrees of freedom are four and one complex phase is contained.

Of the unitary conditions for each columns,

$$V_{ud}V_{ub}^* + V_{cd}V_{cb}^* + V_{td}V_{tb}^* = 0 \tag{2.9}$$

is most famous, since the three terms have the same orders of magnitude and that can be studied with B meson decays. This condition is equivalent to the triangle in the complex plane, called "Unitarity Triangle" (Figure 2.1), and the angles are defined as

$$\phi_1 \equiv \pi - \arg\left(\frac{-V_{td}V_{tb}^*}{-V_{cd}V_{cb}^*}\right), \tag{2.10}$$

$$\phi_2 \equiv \arg\left(\frac{V_{td}V_{tb}^*}{-V_{ud}V_{ub}^*}\right), \tag{2.11}$$

$$\phi_3 \equiv \arg\left(\frac{V_{ud}V_{ub}^*}{-V_{cd}V_{cb}^*}\right). \tag{2.12}$$

The measurement of these angles as well as the lengths of the sides of the Unitarity Triangle are the crucial test of the CKM picture of the CP violation, which is the fundamental part of the Standard Model. Also, the studies of those parameters may reveal new physics.
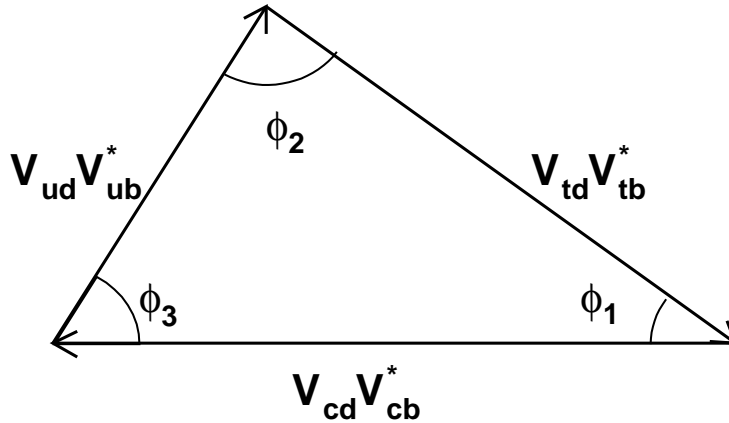
Figure 2.1: Unitarity Triangle.

2.2 Determination of ϕ_3

By the definition of Eq. (2.12), ϕ_3 does not depend on CKM elements involving the top quark, so it can be measured in tree level B decays [7]. Therefore, the measurements of ϕ_3 are unlikely to be affected by physics beyond the Standard Model, which is different to the measurements of ϕ_1 and ϕ_2.

The extraction of ϕ_3 is challenging even with modern high luminosity B factories, because a measurement of ϕ_3 needs a diagram which contains V_{ub} and it strongly suppresses the decay amplitude. From Eq. (2.8) and (2.12), ϕ_3 is given as

$$\phi_3 \sim \arg(V_{ub}^*), \tag{2.13}$$

where V_{ub} is the only one that has a complex phase in the expression. Therefore, the measurement of ϕ_3 is equivalent to the measurement of the phase of V_{ub}.

2.2.1 $B^{\pm} \to DK^{\pm}$

Several methods for measuring ϕ_3 use the interference between $B^- \to \bar{D}^0 K^-$ $(b \to u)$ and $B^- \to D^0 K^-$ $(b \to c)$, for which there are no penguin diagrams because of the odd numbers of charm quarks. The interference occurs when $\bar{D}^0$ and D^0 decay to common final states. In principle, we can extract the B and D decay amplitudes, the relative strong phases, and the weak phase ϕ_3. Throughout this section, the possibility of D^0-$\bar{D}^0$ mixing is neglected, but its effect on ϕ_3 is far below the present experimental accuracy [8], unless D^0-$\bar{D}^0$ mixing is due to CP-violating new physics, in which case it could be included in the analysis [9].

GLW method

The Gronau-London-Wyler (GLW) strategy to extract ϕ_3 is to separately determine the branching ratios [10, 11]:

(a) $\mathcal{B}(B^- \to D^0 K^-)$

(b) $\mathcal{B}(B^- \to \bar{D}^0 K^-)$

(c) $\mathcal{B}(B^- \to D_{CP(+)} K^-)$ or $\mathcal{B}(B^- \to D_{CP(-)} K^-)$

together with their conjugates, where $D_{CP(\pm)}$ denote the CP eigenstates $D_{CP(\pm)} = (D^0 \pm \bar{D}^0)/\sqrt{2}$. From the measured values of (a), (b), (c), and the corresponding quantities for the conjugate modes, we can extract ϕ_3 with the strong phase differences.

The value (c) can be observed through the decay to a CP eigenstate such as $K^+ K^-$, $\pi^+ \pi^-$, and $K_S \phi$, and the decay (a) is also measurable through either leptonic or hadronic modes of the D^0. However, this method has a very serious problem in measuring (b) [12]. The detector must distinguish $\bar{D}^0$ from D^0 to determine the decay rate to this mode, but the possible two ways to tag the flavor of $\bar{D}^0$ through semi-leptonic decays and through hadronic decays are both likely to be impractical. The semi-leptonic tag has the problem that there is an overwhelming background from the direct semi-leptonic decay of the B meson, while the hadronic decays have the background decays $B^- \to D^0 K^-$ [i.e. (a)] followed by Cabbibo-suppressed D^0 decays, which seem to have more than matchable magnitudes of the branching ratios since the ratio of the interfering amplitudes

$$r_B \equiv \left| \frac{A(B^- \to \bar{D}^0 K^-)}{A(B^- \to D^0 K^-)} \right| \tag{2.14}$$

is thought to be around 0.1-0.2 [7].

ADS method

To alleviate the smallness of r_B and make the interfering amplitudes comparable in magnitude, the ADS method [12] considers final states where Cabbibo-favored $\bar{D}^0$ and doubly Cabbibo-suppressed D^0 decays interfere. In such cases, the CP-violating effects could be enhanced.

We define the amplitudes for B decays and D decays as follows:

$$A_B \equiv A(B^- \to D^0 K^-), \; A_D \equiv A(D^0 \to \bar{f}), \tag{2.15}$$
$$\bar{A}_B \equiv A(B^- \to \bar{D}^0 K^-), \; \bar{A}_D \equiv A(D^0 \to f). \tag{2.16}$$

The branching ratios for $B^- \to [f]_D K^-$ and $B^+ \to [\bar{f}]_D K^+$ decays, where $[f]_D$ indicates that the state f originates from D^0 or $\bar{D}^0$, are given as

$$\mathcal{B}(B^- \to [f]_D K^-) \;=\; [r_B^2 + r_D^2 + 2 r_B r_D \cos(-\phi_3 + \delta)]|A_B|^2 |A_D|^2, \tag{2.17}$$
$$\mathcal{B}(B^+ \to [\bar{f}]_D K^+) \;=\; [r_B^2 + r_D^2 + 2 r_B r_D \cos(\phi_3 + \delta)]|A_B|^2 |A_D|^2, \tag{2.18}$$

where

$$r_B = \left| \frac{\bar{A}_B}{A_B} \right|, \; r_D \equiv \left| \frac{\bar{A}_D}{A_D} \right|, \; \delta \equiv \delta_B + \delta_D, \tag{2.19}$$

and δ_D is the strong phase difference between the two D decays. The value $|A_B|$ is identical to the square root of (a) and can be measured. If we use single f in which

$|A_D|$ and r_D are known, the above two equations have three unknowns, ϕ_3, r_B, and δ. However, using two final states f_1 and f_2, there are four equations and four unknowns, ϕ_3, r_B, δ_1, and δ_2, which can be solved. Furthermore, we can use multiple decay modes for $D \to f_i$, and ϕ_3 is fitted together with other unknowns.

The decay $B^- \to [K^+\pi^-]_D K^-$ is an especially useful mode for the ADS method. Figure 2.2 shows the diagrams for that decay and the reference decay $B^- \to [K^+\pi^-]_D\pi^-$, both of which are studied in this thesis.

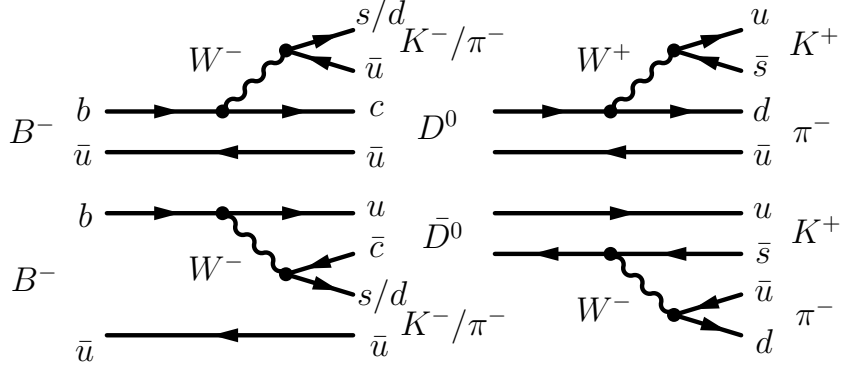Figure 2.2: Diagrams for $B^- \to [K^+\pi^-]_D K^-$ and $B^- \to [K^+\pi^-]_D\pi^-$ decays.

Dalitz analysis

The above approach can be generalized to the case where the D^0 undergoes a three-body, or indeed n-body, decay [12]. The advantage of this method is that it contains all resonant structure of the three-body decay, with interference of doubly Cabbibo-suppressed, Cabbibo-favored, and CP eigenstate amplitudes. The best present determination of ϕ_3 comes from this method, with studying the Dalitz plot dependence on the interferences [13, 14] using the three-body final state of $K_S\pi^+\pi^-$. Belle [15] and BaBar [16] obtained $\phi_3 = 68^{+14}_{-15} \pm 13 \pm 11°$ and $\phi_3 = 67 \pm 28 \pm 13 \pm 11°$, respectively, where the last uncertainty is due to the D decay modeling. This model dependency is too large for the demanded precision of the determination of ϕ_3. We mention that the value r_B, for which we provide a constraint in this thesis, is also appear in this method.

2.2.2 $B \to D^{(*)\pm}\pi^\mp$

Because both B^0 and $\bar{B}^0$ decay to $D^{(*)\pm}\pi^\mp$ (or $D^\pm\rho^\mp$, *etc.*), we can study the interference of $b \to u$ and $b \to c$ transitions using the decays $\bar{B}^0 \to D^{(*)+}\pi^-$ and $\bar{B}^0 \to B^0 \to D^{(*)+}\pi^-$ and the conjugate modes [7]. Basically, we extract $2\phi_1 + \phi_3$ with the strong phase difference and the magnitudes of the hadronic amplitudes. However, there is a problem in this method that the ratio of the interfering amplitudes $r_{D\pi} = A(B^0 \to D^+\pi^-)/A(\bar{B}^0 \to D^+\pi^-)$ is very small and $\mathcal{O}(0.01)$. At present, an assumption is used to relate $A(\bar{B}^0 \to D^-\pi^+)$ to $A(\bar{B}^0 \to D_s^-\pi^+)$, and this method is not model independent. The result obtained by combining the $D^\pm\pi^\mp$, $D^{*\pm}\pi^\mp$ and $D^\pm\rho^\mp$ measurements [17] is $\sin(2\phi_1 + \phi_3) = 0.8^{+0.18}_{-0.24}$, which is consistent with the present results for ϕ_1 and ϕ_3.

Chapter 3

Experimental Apparatus

The Belle experiment is based on the KEKB accelerator and the Belle detector, which are located at the High Energy Accelerator Research Organization (KEK) in Japan.

3.1   KEKB Accelerator

Figure 3.1 shows a schematic layout of the KEKB accelerator [18]. That is a e^+e^- collider, which has two rings for each beam. The energy of e^+ is 8.0 GeV and the one of e^- is 3.5 GeV, which corresponds to the resonance of $\Upsilon(4S)$. Since more than 96% of $\Upsilon(4S)$ decays to $B\bar{B}$ pairs at 95% C.L. [7], many B mesons are produced by the immediate decay of $\Upsilon(4S)$. The accelerator thus is sometimes called the "B factory," and in this thesis we use the data samples containing $657{\times}10^6$ $B\bar{B}$ pairs which corresponds to the time-integrated luminosity[1] of 605 fb^{-1}.

3.2   Belle Detector

The Belle detector [19], shown in Figure 3.2, is a large-solid-angle magnetic spectrometer that consists of a silicon vertex detector (SVD), a 50-layer central drift chamber (CDC), an array of aerogel threshold Cherenkov counters (ACC), a barrel-like arrangement of time-of-flight scintillation counters (TOF), and an electromagnetic calorimeter comprised of CsI(Tl) crystals (ECL) located inside a super-conducting solenoid coil that provides a 1.5 T magnetic field. An iron flux-return located outside of the coil is instrumented to detect K_L^0 mesons and to identify muons (KLM). Two inner detector configurations were used. A 2.0 cm beam pipe and a 3-layer silicon vertex detector was used for the first sample of $152 \times 10^6 B\bar{B}$ pairs, while a 1.5 cm beam pipe, a 4-layer

---

[1]The luminosity is expressed by

$$\mathcal{L} = \frac{N_+ N_- f}{4\pi\sigma_x^*\sigma_y^*},\tag{3.1}$$

where $N_\pm$ is the number of particle $e^\pm$ per bunch, which is the aggregate of $e^\pm$ and an unit of collision, f is the collision frequency, and $\sigma_{x,y}^*$ is the beam size at IP in x or y direction.
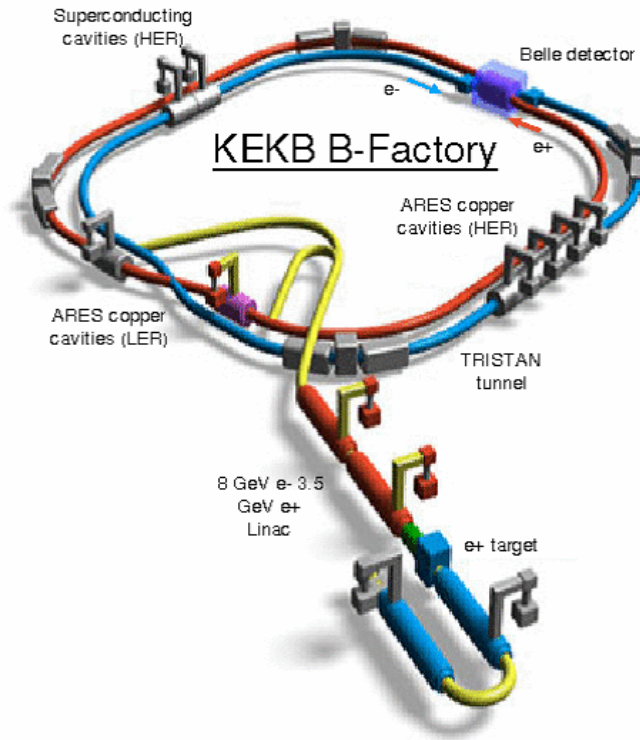
Figure 3.1: KEKB accelerator.

silicon detector and a small-cell inner drift chamber were used to record the remaining $505 \times 10^6 B\bar{B}$ pairs [20].

In the following, we show some details about several parts of the detector which are related to the analysis in this thesis. The descriptions are based on Ref. [19, 20]. The coordinates are defined as in Figure 3.3.

3.2.1   Sillicon Vertex Detector (SVD)

The main purpose of the SVD is to determine the decay vertices of B mesons. This ability has contributed to the time-dependent analyses of B^0 and $\bar{B}^0$ mesons, which revealed the CP asymmetries. On the other hand, the SVD is used as a tracking device in this thesis, while that is mainly based on the measurement at the CDC.

Figure 3.4 shows the configuration of the SVD (SVD1) used up to summer in 2003. The three layers of silicon sensors cover a polar angle of $23° < \theta < 139°$, which corresponds to 86% of the full solid angle of $\Upsilon(4S)$. When a charged particle passes through, it creates ionization in the bulk of the silicon and frees electrons from the atoms with the electron vacancies called holes. The electrons and holes drift in the electromagnetic field to the strips, which are connected to the readout systems. The strips construct the double-sided silicon strip detectors (DSSDs). One side (n-side) of DSSD has strips oriented perpendicular to the beam direction to measure the z coordinate, and the other side (p-side) with longitudinal strips allows the ϕ coordinate measurement.
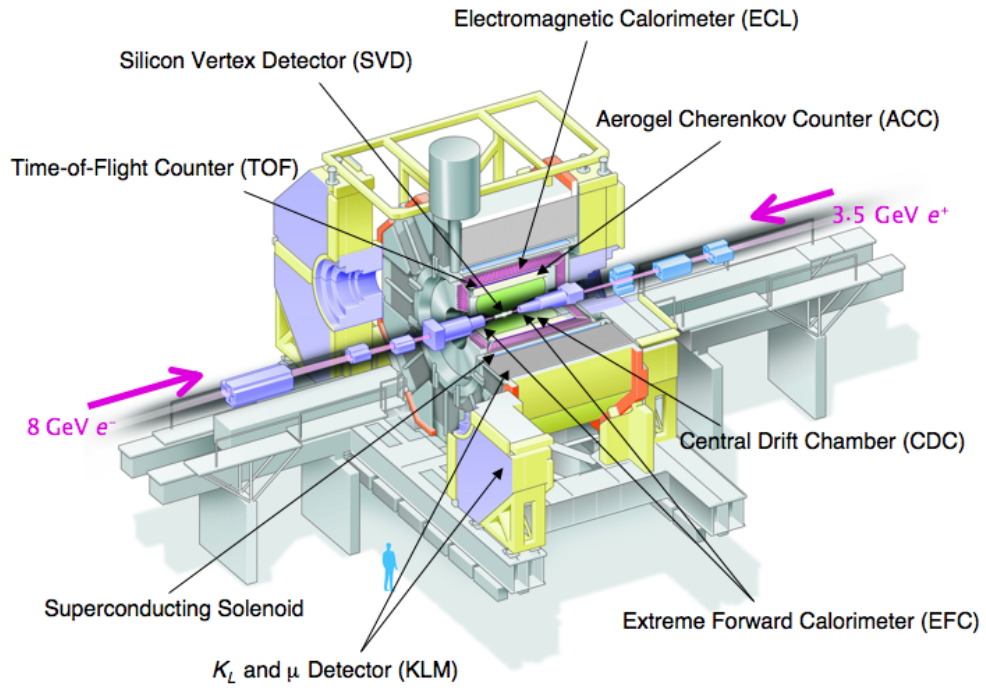
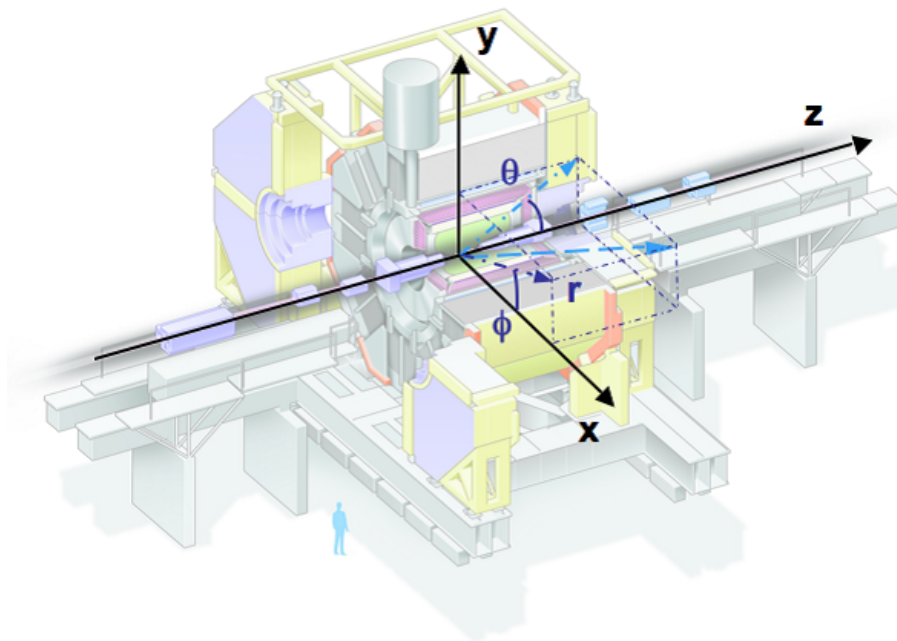Figure 3.2: Overview of the Belle detector.

Figure 3.3: The definition of the Belle coordinates.

In summer of 2003, a new vertex detector, SVD2, was installed [20]. Figure 3.5 shows the configuration of SVD2. It has larger coverage than SVD1, $17° < \theta < 150°$, which is the same as CDC and corresponds to the 92% of the full solid angle. The first layer is closer than SVD1's first layer, which is enabled by a new smaller (1.5 cm in radius) beam pipe.

The resulting SVD-CDC track matching efficiency is better than 98.7% in average, although a slight degradation by the radiation damage is observed.
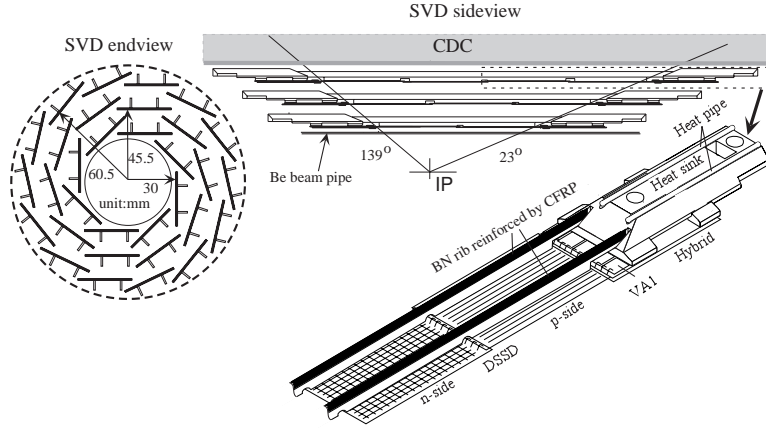
Figure 3.4: Configuration of SVD1.
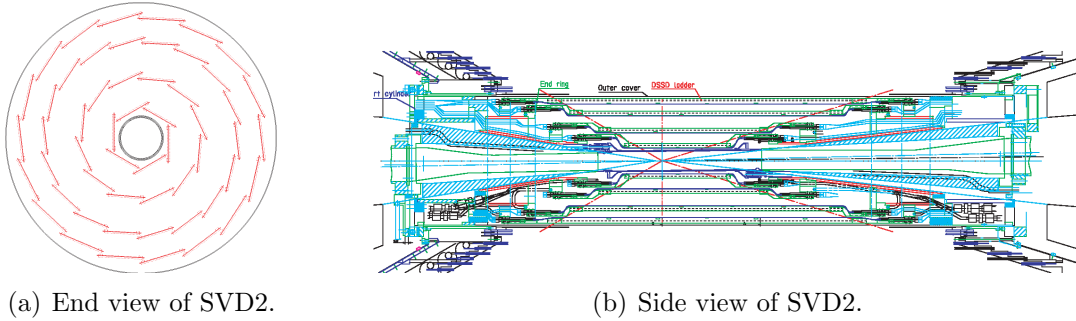
(a) End view of SVD2.   (b) Side view of SVD2.

Figure 3.5: Configuration of SVD2.

3.2.2   Central Drift Chamber (CDC)

The measurements of the momenta of the charged particles is a fundamental issue of the Belle experiment, for which the CDC plays a very important role. The CDC also provide us an information of the energy deposit dE/dx, which can be used for the particle identifications.

Figure 3.6 shows the structure of the CDC. That is a small-cell drift chamber containing of 50 anode and three cathode layers. The anode layers are divided to 32 axial

wires and 18 stereo wires. The former enables us to measure r and ϕ coordinates, and the latter is for z coordinate. For the gas, a low-Z gas mixture consisting of 50% He and 50% ethane (C_2H_6) is used. That keeps the multiple Coulomb scattering at low level, and provides us a good momentum resolution. When a charged particle passes through, the gases are ionized and frees the electrons. The wires capture those electrons, and we construct the tracks from the informations of the positions. The tracks curve in the 1.5T magnetic field provided by the superconducting solenoid, from which we measure the momenta (p_t) transverse to the beam axis. Combining the z coordinate measurements, we can determine the three dimensional momenta. The energy deposit dE/dx is determined from the quantities of the electrons captured by the wires.

The resolution of p_t can be fitted as a function of p_t itself, and is required to be $\sigma_{p_t}/p_t \sim 0.5\%\sqrt{p_t^2 + 1}$ (p_t in GeV/c) for all charged particles with $p_t \geq 100$ MeV/c. Figure 3.7 (a) shows the p_t resolution distributions for cosmic rays and the $\beta = 1$ particle as the ideal expectation. The required performance are actualized. In Figure 3.7 (b), the dE/dx distribution on the momentum of the particle is shown with the expected mean energy deposits. Clear separations in the lower momentum regions are found.
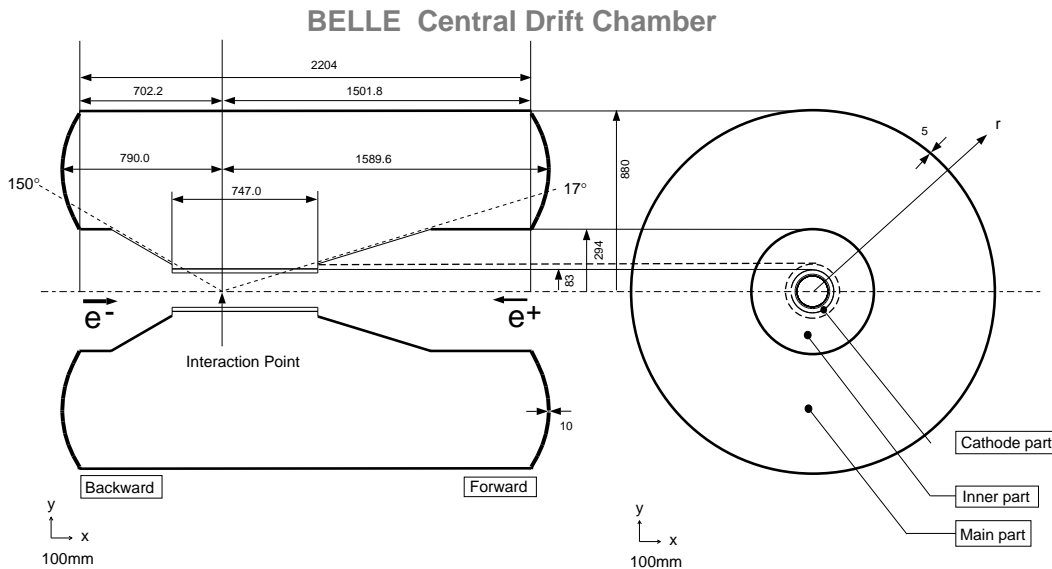
Figure 3.6: Overview of the CDC structure. The lengths in the figure are in units of mm.

3.2.3 Aerogel Cherenkov Counter (ACC)

The identification of $K^\pm$ and $\pi^\pm$ is very important in the Belle experiment. However, the measurement of the energy deposit of the charged particles at CDC and the time-of-flight determination by TOF (see Section 3.2.4) cannot cover the full demanded momentum region. The ACC is constructed to compensate the momentum range of 1.5-3.5 GeV/c.
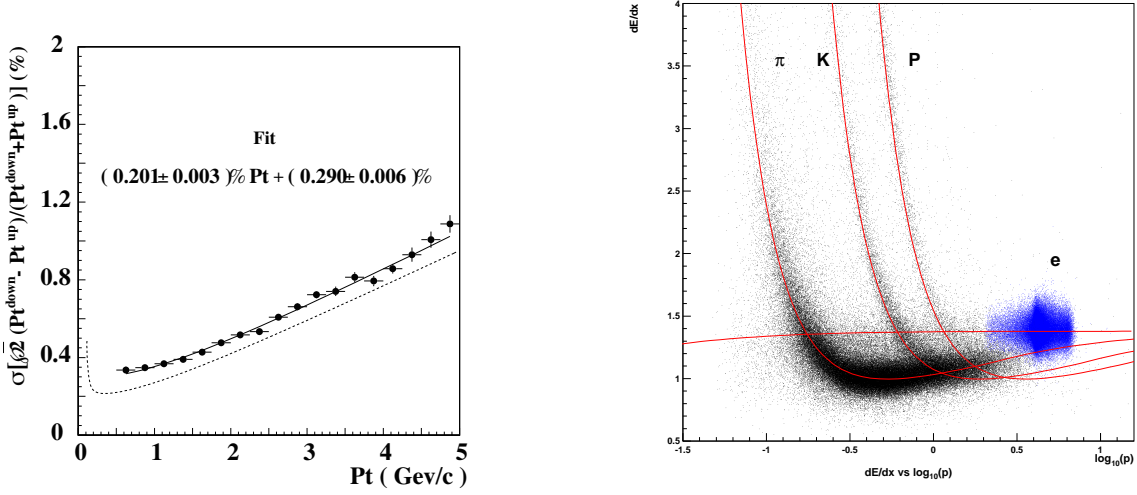
(a) p_t dependence of p_t resolution for cosmic-rays. The solid curve shows the fitted result, and the dotted curve shows the ideal expectation for $\beta = 1$ particle.

(b) Charged track momenta vs. dE/dx observed in collision data.

Figure 3.7: The performances of CDC.

Figure 3.8 shows the configuration of ACC. It consists of 960 counter modules for the barrel part and 228 modules for the end-cap part. All of the counters are arranged in a semi-tower geometry, pointing to IP. If the particle has the velocity β larger than $1/n$, where n is the refractive index of the aerogel, Cherenkov radiations are emitted. That is equivalent to the condition

$$n > \frac{1}{\beta} = \sqrt{1 + \left(\frac{m}{p}\right)^2}, \tag{3.2}$$

where m is the mass of the charged particle. The index n is selected so that the $\pi^{\pm}$ provides the Cherenkov light while $K^{\pm}$ does not. The choices of Belle are from 1.01 to 1.03 depending on their polar angle region, which corresponds to the required coverage of the momentum.

The performance of the ACC is checked using the decay $D^{*-} \rightarrow D^0 \pi^-$ followed by $\bar{D}^0 \rightarrow K^+ \pi^-$. This decay can be reconstructed without the particle identification. The K^+ and π^- can be separated with the charges of the particles, and π^- directly from D^{*-} is distinguished by the characteristic low momentum of itself based on the small mass difference of D^{*-} and D^0. Figure 3.9 shows the number of photo-electron distribution for π^- and K^+ from D^{*-} decays. Each plot corresponds to the different set of modules with a different n. Good K/π separations can be seen.
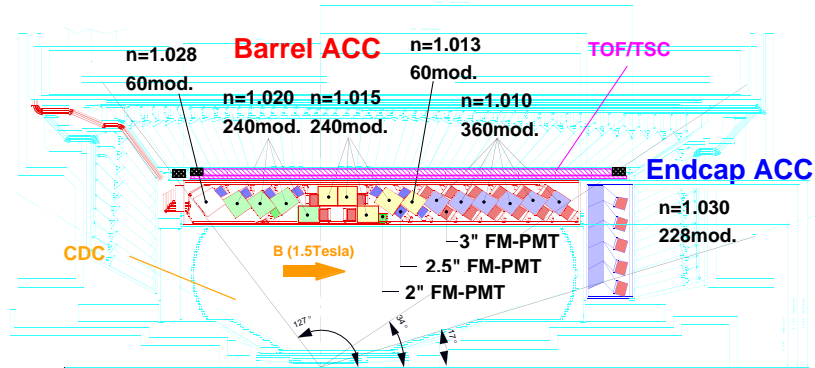
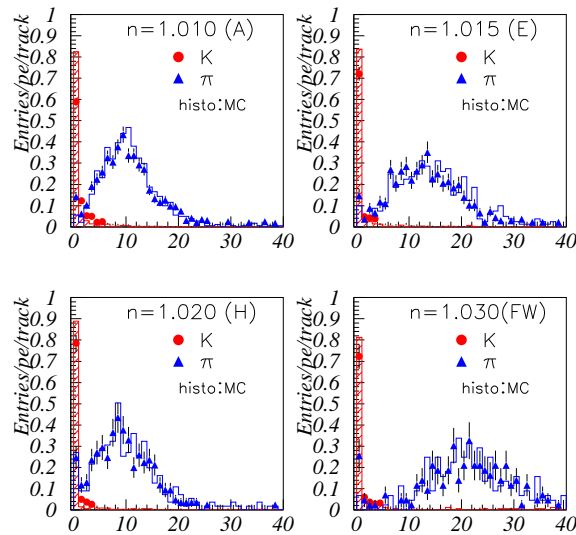Figure 3.8: The arrangement of ACC at the central part of the Belle detector.

Figure 3.9: ACC number of photo-electron distribution for $\pi^{\pm}$ and $K^{\pm}$ from $D^{*\pm}$ decays. Each plot corresponds to the different set of modules with a different refractive index

3.2.4   Time-of-Flight Counter (TOF)

The time-of-flight information provided by the TOF can be used for the particle iden-tification. Measured time T is related to path length L, velocity β, momentum p, and mass m of the particle as

$$T = \frac{L}{c\beta} = \frac{L}{c}\sqrt{1 + \left(\frac{m}{p}\right)^2}. \tag{3.3}$$

Thus, combining the value of p measured at CDC, we can determine the mass of the particle.

The TOF system is based on two types of plastic scintillation counters, which are the TOF counter and the trigger scintillation counter (TSC). Figure 3.10 shows the dimension of the module. Two TOF counters and one TSC make a module, where the 1.5 cm gap between the TOF counters and TSC is on purpose of isolating TOF from photon conversion backgrounds by taking the coincidence. There are 64 modules in total, and those also contribute to the trigger system.

The time resolution of 100 ps is required, because that corresponds to the effective identification of particles with momenta below 1.2 GeV/c, which encompasses 90% of the particles produced in $\Upsilon(4S)$ decays. Figure 3.10 (a) shows the resolution as a function of z for $e^+e^- \to \mu^+\mu^-$ events. Combining the informations in forward and backward readout systems, the demanded resolution is actualized. Figure 3.10 (b) shows the mass distribution from TOF measurements for the particles with momenta below 1.2 GeV/c. Clear peaks corresponding to $\pi^\pm$, $K^\pm$, and protons are seen.
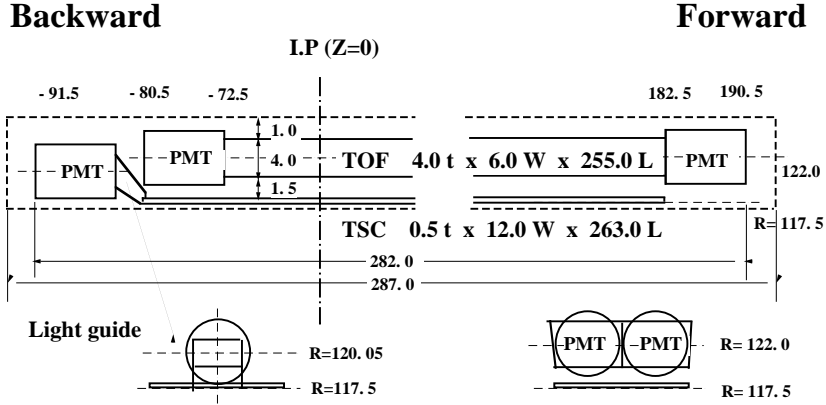

Figure 3.10: Dimension of a TOF/TSC module.

3.2.5   Solenoid Magnet

The curvature of the track, which is used for the transverse momentum measurement, is based on the 1.5 T magnetic field provided by the superconducting solenoid. We determine p_t from

$$p_t = qBr, \tag{3.4}$$

(a) Time resolution of TOF for $e^+e^- \to \mu^+\mu^-$ events.

(b) Mass distribution from TOF measurements for particle momenta below 1.2 GeV/c.
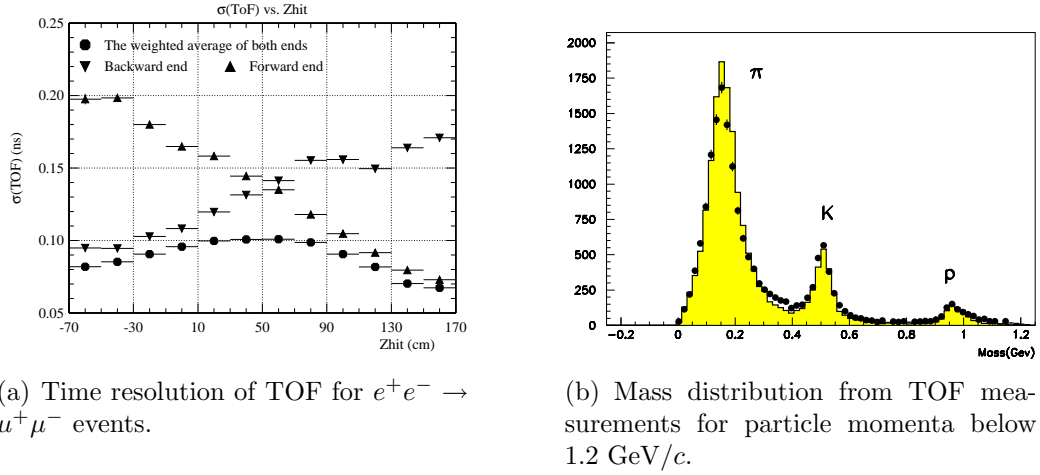
Figure 3.11: TOF performances.

where q is the charge of the particle, B is the magnetic field, and r is the curvature radius.

Figure 3.12 shows an outlook of the solenoid and the cross-sectional view of the coil. The solenoid has a cylindrical volume of 3.4 m in diameter and 4.4 m in length. The superconductor is NbTi/Cu, and Al is used for 99.99% of the stabilizer. The coil is surrounded by a multilayer structure which consists of the iron plates and calorimeters.

(a) Outlook of the magnet

(b) Cross sectional view of the coil

Figure 3.12: An outlook of the solenoid and the cross-sectional view of the coil.

3.2.6   Trigger and Data Acquisition Systems

Trigger (TRG) System

The physics events of our interest, $e^+e^- \to B\bar{B}$, is smaller in cross section than the background of $e^+e^- \to q\bar{q}$ $(q = u, d, s, c)$. Figure 3.13 shows the cross section distribution around the Υ resonances. It's easy to see many backgrounds under the $\Upsilon(4S)$ peak. To reject those processes, fast trigger system is needed.
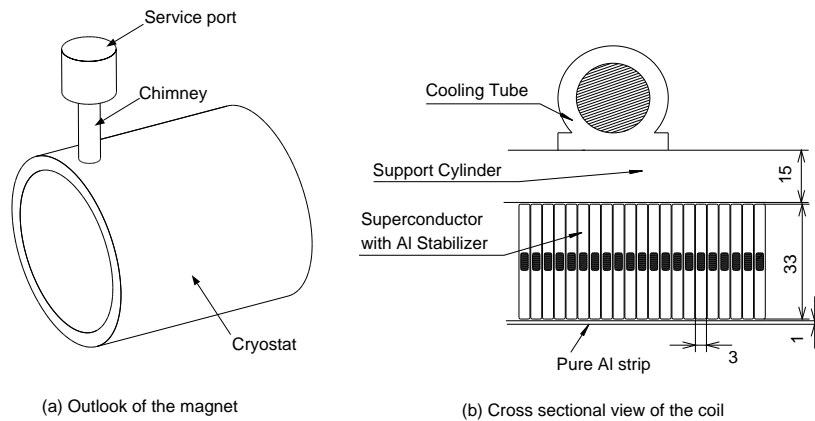
The Belle trigger system contains the Level-1 hardware trigger and the Level-3 software trigger. Figure 3.14 shows the schematic view of the Belle Level-1 trigger system. The information of sub-triggers from several sub-detectors are combined to characterize the event type in the central trigger system called the Global Decision Logic (GDL). The Level-3 software trigger is designed to be implemented in the online computer farm. A decision for the trigger is made within 2.2 μs after the beam collision at IP.
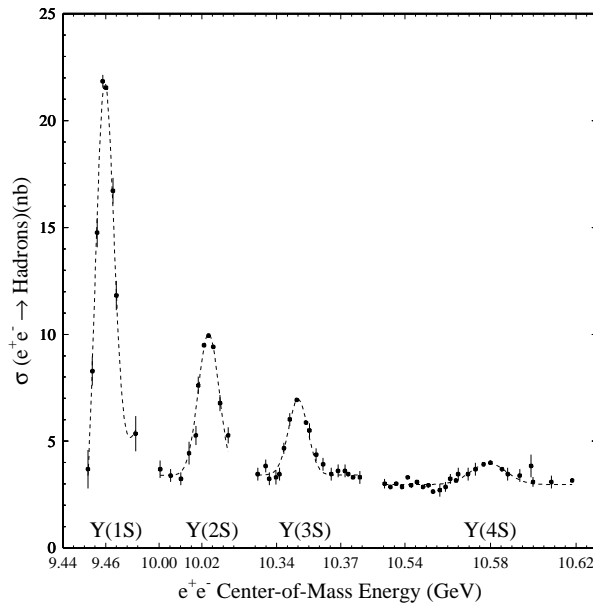
Figure 3.13: The cross-section of the process $e^+e^- \to$ hadron. There are many backgrounds from $e^+e^- \to q\bar{q}$ $(q = u, d, s, c)$ in the region of the $\Upsilon(4S)$ resonance.

Data Acquisition (DAQ) System

The DAQ of Belle uses the distributed-parallel system for achieving low dead times with high frequencies. Figure 3.15 shows the schematic view of the DAQ. There are seven subsystems for each sub-detector. The data from the subsystems are combined, and the "detector-by-detector" parallel data are converted to the "event-by-event" data river. The output of the event builder is transported to an online computer farm, where an event filtering with fast event reconstruction is done. Then the data are sent to a mass storage system.

Belle Trigger System

SVD	Rφ	Rφ Track			
	Z	Z Track			
CDC	Cathod Pads			Combined Track	
	Stereo Wires	Z Finder	Z Track		
	Axial Wires	Track Segment	Rφ Track	Topology	
TSC	Hit	TSC Trigger		Timing	
ECL	4x4 Sum	Low Threshold	Cluster Count		
		High Threshold	Cluster Count		
		E Sum	Threshold		
EFC	Amp.	Low Threshold	Bhabha Logic		
		High Threshold	Two γ Logic		
KLM	Hit	□ hit			

Global Decision Logic

Trigger Signal
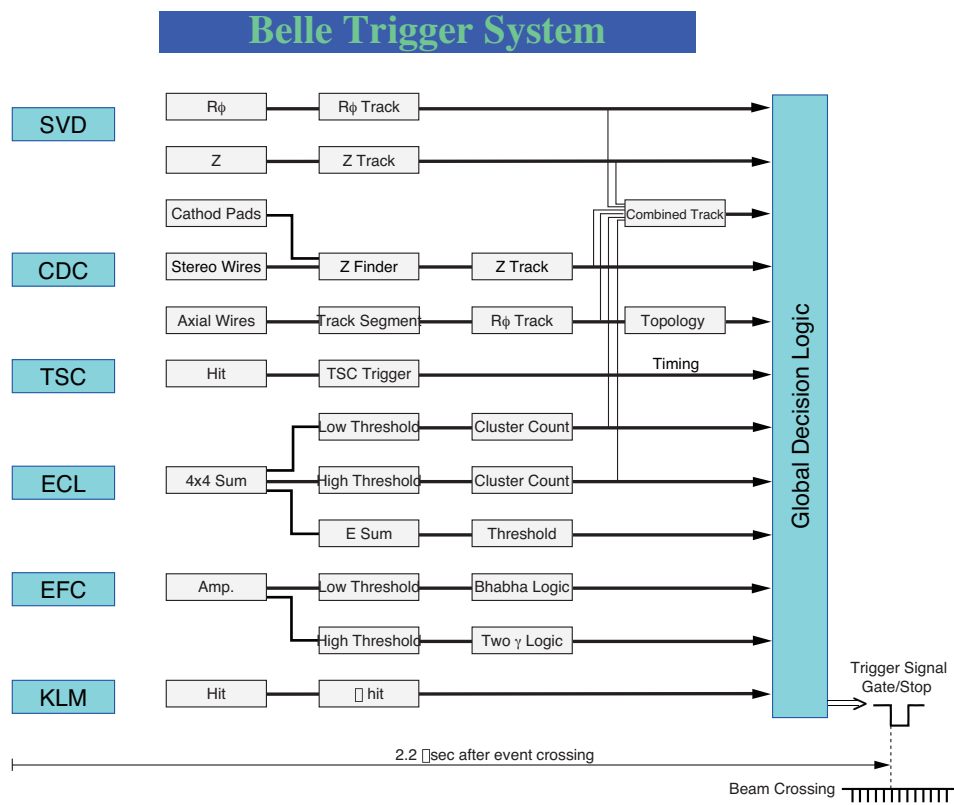Gate/Stop

2.2 □sec after event crossing

Beam Crossing

Figure 3.14: The Level-1 trigger system for the Belle detector.
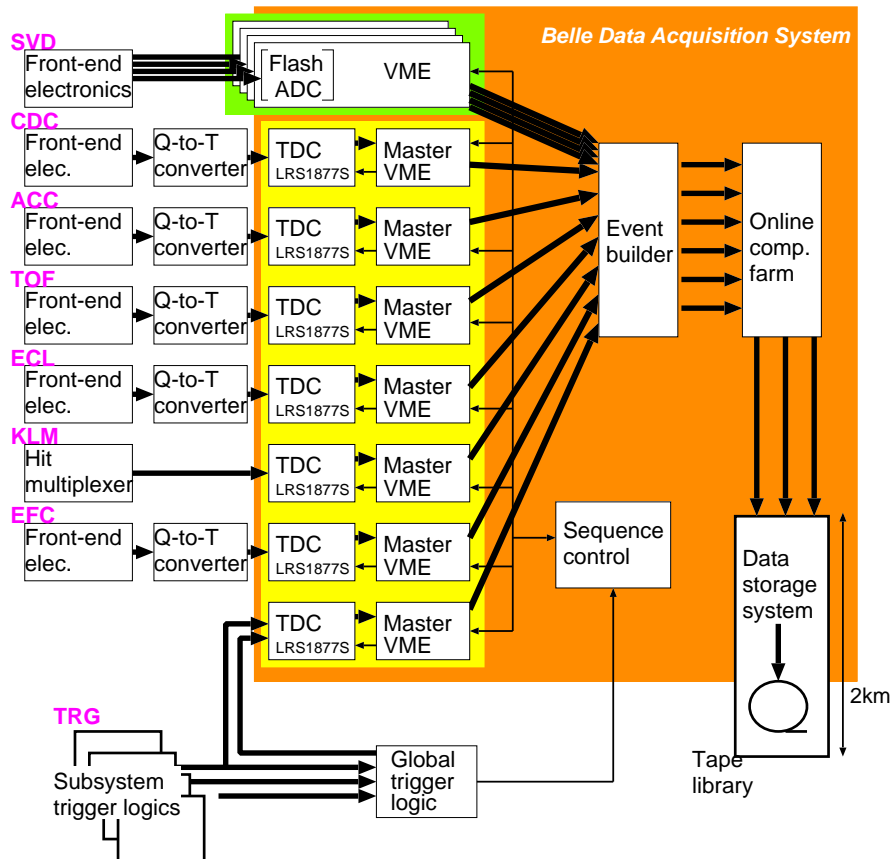
Figure 3.15: Belle DAQ system overview.

Chapter 4

Event Selection and Signal Extraction

In this analysis, we measure the ratios of the suppressed decays $B^- \to [K^+\pi^-]_D h^-$ over the favored decays $B^- \to [K^-\pi^+]_D h^-$, where $h = K$ or π, in order to cancel systematic errors. The same selection criteria are used for the suppressed decays and the favored decays whenever possible. We denote the decays $B^- \to [K^+\pi^-]_D h^-$ as $B^- \to D_{\text{sup}} h^-$, and the decays $B^- \to [K^-\pi^+]_D h^-$ as $B^- \to D_{\text{fav}} h^-$. Furthermore, K^- or π^- that originates directly from B^- is referred to as the 'prompt' particle. We note that the charge conjugate reactions are implied in the following, except where explicitly mentioned.

Basically, we reconstruct the signal decay candidates with several requirements for the rejection of the backgrounds, and fit the distribution of a kinematical value ΔE, which is mentioned in the section 4.3.3, with a function containing signal component. The requirements and the fitting procedure are decided without looking at the data sample in the signal region. This kind of analysis is called the "Blind analysis" and is the optimal way to reduce or eliminate experimenter's bias, the unintended biasing of a result in a particular direction.

4.1 Data Set

The analysis presented in this thesis is based on a $\Upsilon(4S)$ resonance data sample taken from January 2000 to December 2006. The integrated luminosity is 605 fb^{-1}, which contains 657×10^6 $B\bar{B}$ pairs.

4.2 $K^\pm/\pi^\pm$ Identification

Our reconstructions of the events are based on the identifications of $K^\pm$ and $\pi^\pm$, which are the daughter particles of the decays analyzed. We determine the momenta of those particles with the track curvatures, but we don't measure the energies. We identify the particles and assign invariant masses, from which we calculate the energies.

We discriminate between $K^\pm$ and $\pi^\pm$ by combining the informations from ACC and TOF and specific ionization measurements from CDC. The probability density functions are modeled for each-detector measurements and for each of $K^\pm$ and $\pi^\pm$, and then the likelihood functions are calculated. From those functions, we obtain likelihoods for $K^\pm$ ($\mathcal{L}_K$) and for $\pi^\pm$ ($\mathcal{L}_\pi$) for each track. Finally, we provide requirements based on the likelihood ratio defined as

$$P(K/\pi) \equiv \frac{\mathcal{L}_K}{\mathcal{L}_K + \mathcal{L}_\pi} \tag{4.1}$$

and identify as $K^\pm$ or $\pi^\pm$.

The decay chain of $D^{*-} \to \bar{D}^0 \pi^-$ followed by $\bar{D}^0 \to K^+ \pi^-$ can be reconstructed without particle identification requirements (section 3.2.3) and used for demonstrate the validity of the $K^\pm/\pi^\pm$ identification. Figure 4.1 shows a two-dimentional distribution of $P(K/\pi)$ and momenta for the tracks of $K^\pm$ and $\pi^\pm$. Clear separation up to $\sim$4 GeV/c can be seen. This is realized by the different momentum coverages of each sub-detector shown in Figure 4.2
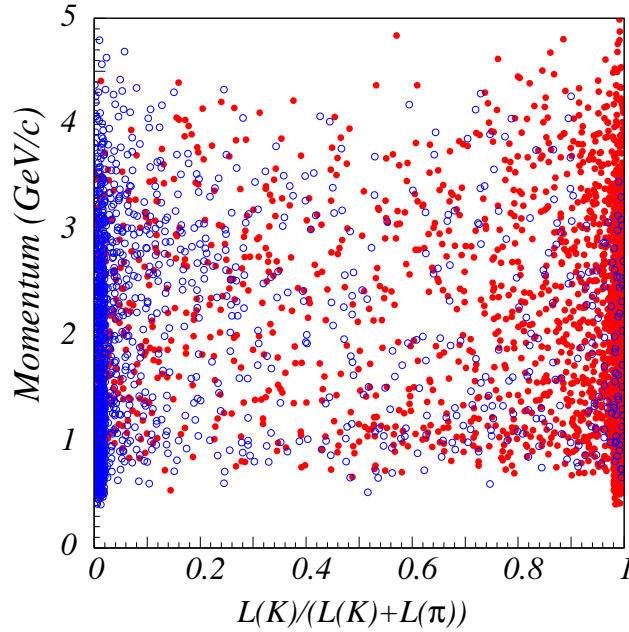

Figure 4.1: A scatter plot of the track momentum (vertical axis) and the likelihood ratio $P(K/\pi)$ (horizontal axis) for $K^\pm$ (closed circle) and $\pi^\pm$ (open circle) obtained from the data of the decay chain $D^{*-} \to \bar{D}^0 \pi^-$ followed by $\bar{D}^0 \to K^+ \pi^-$. Strong concentration in the region of $P(K/\pi) \sim 1$ (~ 0) is observed for $K^\pm$ ($\pi^\pm$) over a wide momentum region up to ~ 4 GeV/c.
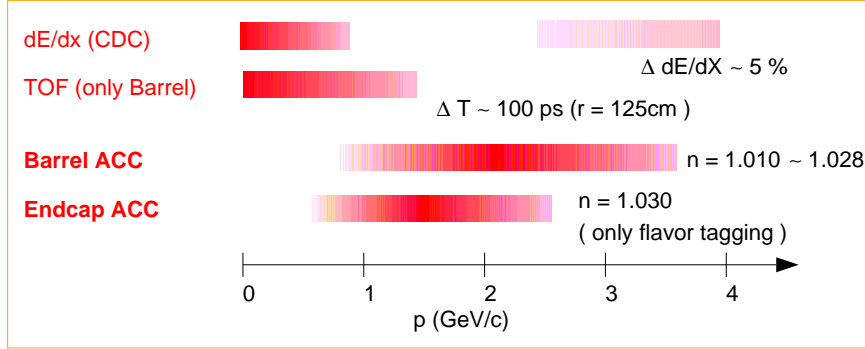
Figure 4.2: Momentum coverage of each detector used for $K^{\pm}/\pi^{\pm}$ separation.

4.3 Event Selection

4.3.1 Charged Tracks

All candidate tracks are required to have a point of closest approach to the beam line within $\pm$ 5 mm of IP in the direction perpendicular to the beam axis (dr) and $\pm$ 5 cm in the direction parallel to the beam axis (dz), because B and D make very short flights.

- $\mid dr \mid <$ 5 mm, $\mid dz \mid <$ 5 cm

4.3.2 D Reconstruction

A neutral D meson is reconstructed by combining two oppositely charged tracks. We use the particle identification requirement $P(K/\pi) > 0.4$ for kaon candidate and $P(K/\pi) < 0.7$ for pion candidate. The efficiency of this requirement for a kaon (pion) is 92% (94%), while the probability that a pion (kaon) is misidentified as a kaon (pion) is 15% (20%). The D meson candidates are demanded to have an invariant mass within $\pm 3\sigma$ of the nominal D mass, where the value σ is the resolution of the D mass and 0.015 GeV/c^2.

- K tracks : $P(K/\pi) > 0.4$

- π tracks : $P(K/\pi) < 0.7$

- $\mid M(K\pi) - 1.865$ GeV/$c^2 \mid <$ 0.015 GeV/c^2

To improve the momentum determinations, tracks from the D candidate are refitted with the invariant mass constrained to the nominal D mass. Even though D vertex constraint is also tried, the improvement is not significant and thus not used (Figure 4.3)[1].

---

[1]The track of a particle is determined by minimizing the χ^2 obtained using the experimental resolutions of each hit point in the detector. The mass and vertex constraints here are to fix the tracks with minimizing χ^2 under the conditions that the mass should be the nominal one and the tracks make a point of vertex, respectively.
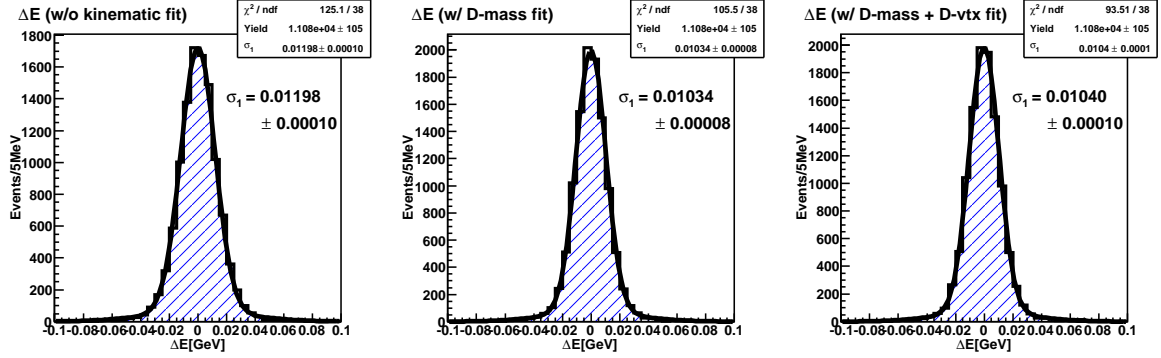
Figure 4.3: The ΔE distributions for Monte Carlo sample with $B^- \to D_{\mathrm{sup}}K^-$ selection. No kinematic fit is applied in the left figure, D mass constraint is applied in the center one, and D mass and D vertex fits are applied in the right one.

4.3.3 B Reconstruction

A B meson is reconstructed by combining a D candidate with a prompt charged hadron candidate, for which a particle identification requirement of $P(K/\pi) > 0.6$ ($P(K/\pi) < 0.2$) is used for $B^- \to DK^-$ ($B^- \to D\pi^-$). With this requirement, the efficiency for a kaon (pion) is 84% (79%), while the probability that a pion (kaon) is misidentified as a kaon (pion) is 10% (9%). The signal is identified by two kinematic variables, the beam-energy-constrained mass $M_{\mathrm{bc}} = \sqrt{E_{\mathrm{beam}}^2 - |\vec{p}_D + \vec{p}_{h^-}|^2}$, and the energy difference $\Delta E = E_D + E_{h^-} - E_{\mathrm{beam}}$, where E_{beam} is the beam energy in the center-of-mass (c.m.) frame. We require M_{bc} to be within $\pm 3\sigma$ of the nominal B mass, while the ΔE distribution is fitted to extract the signal yield. The ΔE distributions for the Monte Carlo signals are shown in the Figure 4.4, which shows that the same shape can be used for all modes.

- prompt K tracks : $P(K/\pi) > 0.6$

- prompt π tracks : $P(K/\pi) < 0.2$

- $| M_{\mathrm{bc}} - 5.279 \ \mathrm{GeV}/c^2 | < 0.008 \ \mathrm{GeV}/c^2$

In the rare cases where there are more than one candidates in an event (0.3% for $B^- \to D_{\mathrm{sup}}K^-$ and 0.7% for $B^- \to D_{\mathrm{sup}}\pi^-$), we select the best candidate on the basis of a χ^2 determined from the difference between the measured values of $M(K\pi)$ and M_{bc} and the nominal masses of D^0 and B^- as

$$\chi^2 = \left(\frac{M(K\pi) - 1.865 \ \mathrm{GeV}/c^2}{\sigma_{M(K\pi)}}\right)^2 + \left(\frac{M_{bc} - 5.279 \ \mathrm{GeV}/c^2}{\sigma_{M_{bc}}}\right)^2, \tag{4.2}$$

where $\sigma_{M(K\pi)}$ and $\sigma_{M_{bc}}$ represent experimental resolutions for $M(K\pi)$ and M_{bc}, respectively.
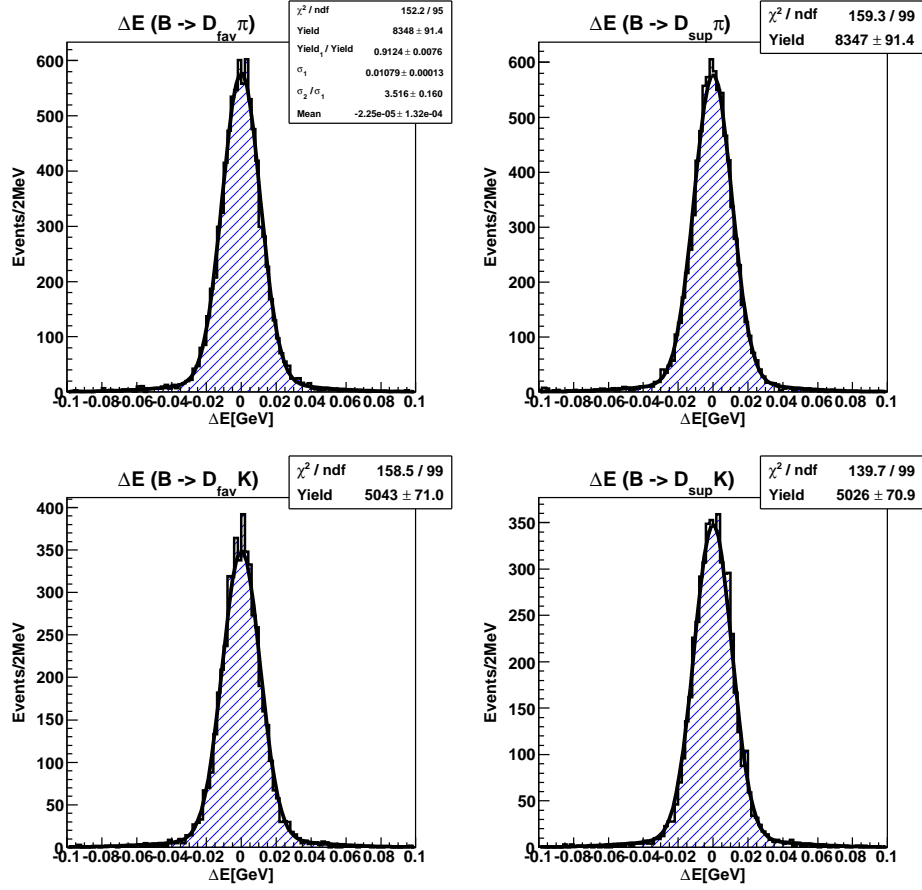
Figure 4.4: The ΔE fit for the Monte Carlo signal of $B^- \to D_{\mathrm{fav}}\pi^-$ (top-left), $B^- \to D_{\mathrm{sup}}\pi^-$ (top-right), $B^- \to D_{\mathrm{fav}}K^-$ (bottom-left), and $B^- \to D_{\mathrm{sup}}K^-$ (bottom-right). A sum of two Gaussians is used for each. All the parameters are free for $B^- \to D_{\mathrm{fav}}\pi^-$, while the shape parameters are fixed to that result for all other modes.

4.3.4 $q\bar{q}$ Background Suppression

To suppress the large background from the two-jet-like $e^+e^- \rightarrow q\bar{q}$ ($q = u, d, s, c$) continuum processes[2], variables that characterize the event topology are employed. We use a Fisher discriminant [21] of modified Fox-Wolfram moments called the Super-Fox-Wolfram (SFW) [22] and $\cos\theta_B$, where θ_B is the angle of the B flight direction with respect to the beam axis in the c.m. system. These two independent variables, SFW and $\cos\theta_B$, are combined to form likelihoods for signal ($\mathcal{L}_{\mathrm{sig}}$) and for continuum background ($\mathcal{L}_{\mathrm{cont}}$), and we constract a likelihood ratio

$$\mathcal{R} = \frac{\mathcal{L}_{\mathrm{sig}}}{\mathcal{L}_{\mathrm{sig}} + \mathcal{L}_{\mathrm{cont}}}. \tag{4.3}$$

Figure 4.5 shows the $\mathcal{R}$ distributions of the signal Monte Carlo sample and of the $q\bar{q}$ background Monte Carlo sample for each mode of $B^- \rightarrow D_{\mathrm{sup}}K^-$ and $B^- \rightarrow D_{\mathrm{sup}}\pi^-$. We optimize the $\mathcal{R}$ requirements using Monte Carlo samples by maximizing $S/\sqrt{S+B}$, where S and B denote the expected numbers of signal and background events in the signal region. Figure 4.6 shows the $S/\sqrt{S+B}$ distributions on the $\mathcal{R}$ requirements. For $B^- \rightarrow D_{\mathrm{sup}}K^-$, we assume three cases $r_B = 0$, $r_B = 0.10$ and $r_B = 0.15$, and take into account only the largest contribution, $B^- \rightarrow \bar{D}^0 K^-$ followed by $\bar{D}^0 \rightarrow K^+\pi^-$, for $r_B = 0.10$ and $r_B = 0.15$. The optimized requirements are

- $\mathcal{R} > 0.90$ for $B^- \rightarrow DK^-$ modes and

- $\mathcal{R} > 0.74$ for $B^- \rightarrow D\pi^-$ modes,

which retains 44.5% (69.5%) of the signal events and removes 99.1% (95.7%) of the continuum background for $B^- \rightarrow D_{\mathrm{sup}}K^-$ ($B^- \rightarrow D_{\mathrm{sup}}\pi^-$).
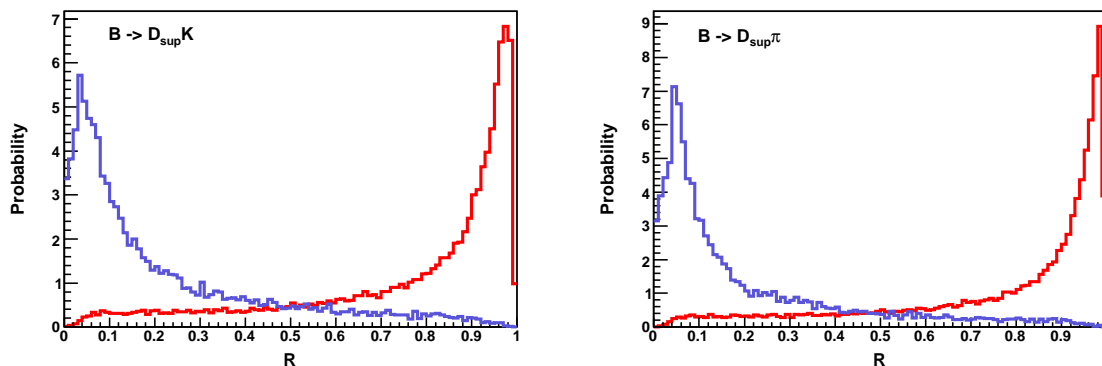

Figure 4.5: $\mathcal{R}$ distributions for $B^- \rightarrow D_{\mathrm{sup}}K^-$ (left) and $B^- \rightarrow D_{\mathrm{sup}}\pi^-$ (right). The red line is for the signal Monte Carlo sample and the blue line is for $q\bar{q}$ Monte Carlo sample.

---

[2]Though the trigger system reject many $q\bar{q}$ backgrounds, a large amount of the backgrounds still remains.
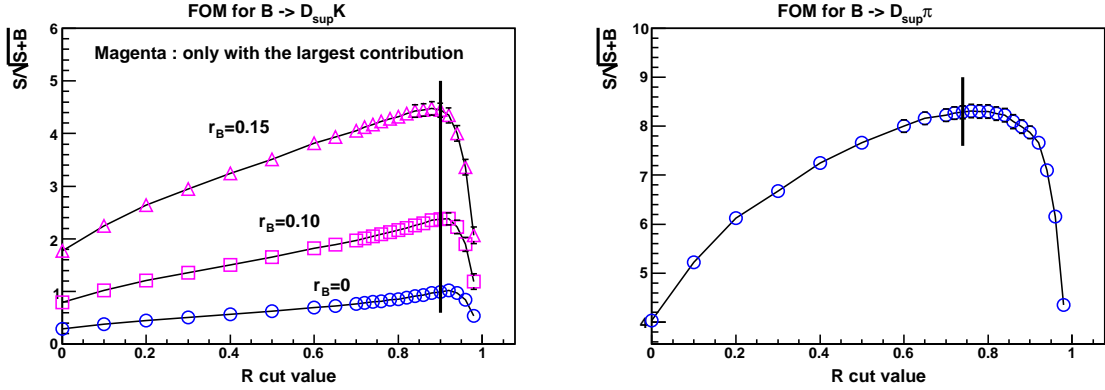
Figure 4.6: Figure of merit distributions for $B^- \to D_{\mathrm{sup}}K^-$ (left) and $B^- \to D_{\mathrm{sup}}\pi^-$ (right).

4.3.5 Peaking Background Suppressions

For $B^- \to D_{\mathrm{sup}}K^-$, there can be a contribution from $B^- \to [K^+K^-]_D\pi^-$, which has the same final state and can peak under the signal in the ΔE fit. In order to reject these events, we require

- $| M(KK) - 1.865 \text{ GeV}/c^2 | > 0.025 \text{ GeV}/c^2$,

where $M(KK)$ is the invariant mass of K^+ and K^-. After such requirement, the estimated number of events which contribute to the signal yield is 0.22 ± 0.19. This value is obtained from $N_{B^-} \times \mathcal{B}(B^- \to [K^+K^-]\pi^-) \times \epsilon_{[K^+K^-]_D\pi^-, D_{\mathrm{sup}}K^-}$, where N_{B^-} is the number of B^- in the data sample used in this thesis, and $\epsilon_{[K^+K^-]_D\pi^-, D_{\mathrm{sup}}K^-}$ is the efficiency of the decay $B^- \to [K^+K^-]_D\pi^-$ in the analysis for $B^- \to D_{\mathrm{sup}}K^-$. The efficiency is obtained as follows: We fit the ΔE distribution of the Monte Carlo sample of $B^- \to [K^+K^-]_D\pi^-$ after $B^- \to D_{\mathrm{sup}}K^-$ selection and the above requirement (Figure 4.7) using a linear function and a sum of two Gaussians which is the same as the one for the fit to $B^- \to D_{\mathrm{sup}}K^-$ signal. Fitted yield is divided by the number of generated B^- in the Monte Carlo sample, which is one million here. The error ± 0.19 is dominated by the uncertainty of the yield from the fit. We subtract the estimated value 0.22 ± 0.19 from the fitted yield of $B^- \to D_{\mathrm{sup}}K^-$, where the loss of the signal efficiency of the requirement is 0.13%.

The favored decay $B^- \to D_{\mathrm{fav}}h^-$ can also cause a peaking background for the suppressed decay modes if both the kaon and the pion from the D_{fav} decay are misidentified and the particle types are exchanged. Therefore, we require

- $| M(K\pi)_{\mathrm{exchanged}} - 1.865 \text{ GeV}/c^2 | > 0.020 \text{ GeV}/c^2$

where $M(K\pi)_{\mathrm{exchanged}}$ is the invariant mass of the $K\pi$ pair under the condition that the mass assignment is exchanged. After that requirement, 0.17 ± 0.13 (6.0 ± 2.1) events are estimated to contribute to the signal yield for $B^- \to D_{\mathrm{sup}}K^-$ $(B^- \to D_{\mathrm{sup}}\pi^-)$. This value is obtained from $N_{B^-} \times \mathcal{B}(B^- \to D_{\mathrm{fav}}h^-) \times \epsilon_{D_{\mathrm{fav}}h^-, D_{\mathrm{sup}}h^-}$, where $\epsilon_{D_{\mathrm{fav}}h^-, D_{\mathrm{sup}}h^-}$

is the efficiency of the decay $B^- \to D_{\text{fav}}h^-$ in the analysis for $B^- \to D_{\text{sup}}h^-$. This efficiency is obtained as follows: We fit the ΔE distribution of a million event Monte Carlo sample of $B^- \to D_{\text{fav}}h^-$ after $B^- \to D_{\text{sup}}h^-$ selection and the above requirement (Figure 4.8, 4.9), and divide the obtained yield by the number of generated B^- in the Monte Carlo sample. The error ± 0.13 (± 2.1) is dominated by the uncertainty of the yield from the fit. We subtract the estimated value 0.17 ± 0.13 (6.0 ± 2.1) from the signal yield, where the efficiency loss by the requirement is 2.0% (3.3%) for $B^- \to D_{\text{sup}}K^-$ ($B^- \to D_{\text{sup}}\pi^-$).
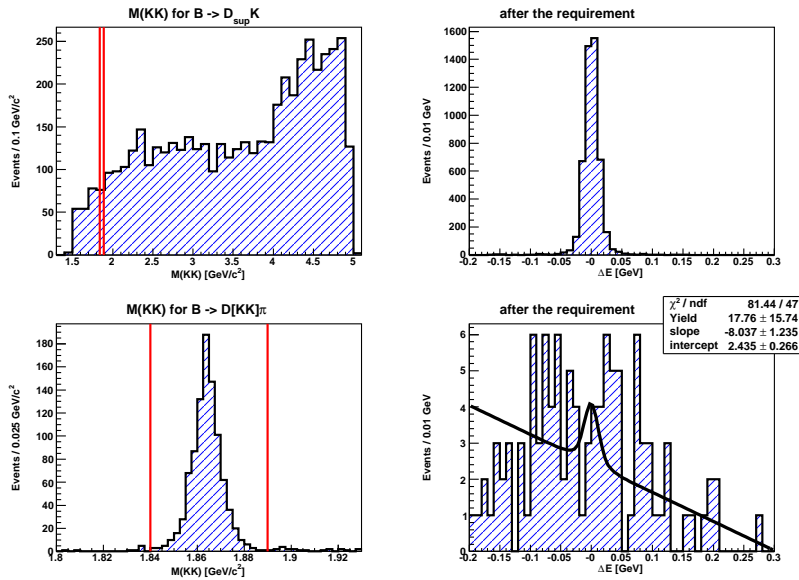

Figure 4.7: The distributions of $M(KK)$ for the $B^- \to D_{\text{sup}}K^-$ Monte Carlo sample (upper-left) and the $B^- \to [K^+K^-]_D\pi^-$ Monte Carlo sample (lower-left) with $B^- \to D_{\text{sup}}K^-$ selection. The red lines show the range of the veto requirement we use. The right figures show the ΔE distributions after the requirement for each sample. We note that the 30,000 and 1,000,000 events are contained in the Monte Carlo samples for $B^- \to D_{\text{sup}}K^-$ and $B^- \to [K^+K^-]_D\pi^-$, respectively.

The charmless decay $B^- \to K^+K^-\pi^-$ ($B^- \to K^+\pi^-\pi^-$) can peak inside the signal region for $B^- \to D_{\text{sup}}K^-$ ($B^- \to D_{\text{sup}}\pi^-$). We don't apply any requirement for the suppression of that background, but we estimate the contribution. We fit the ΔE distribution of events in the D mass sideband[3] data samples, defined as $0.020 \text{ GeV}/c^2 < |M(K\pi) - 1.865 \text{ GeV}/c^2| < 0.080 \text{ GeV}/c^2$, and obtain the expected yield as -2.3 ± 2.4 (2.5 ± 4.5). We regard this contribution as zero and take $+2.4$ ($+4.5$) for a systematic error.

---

[3]We have checked that the ΔE distributions of the D mass signal region and the D mass sideband region of the background have similar resolutions using a Monte Carlo sample for $B^- \to K^+K^-\pi^-$ ($B^- \to K^+\pi^-\pi^-$).
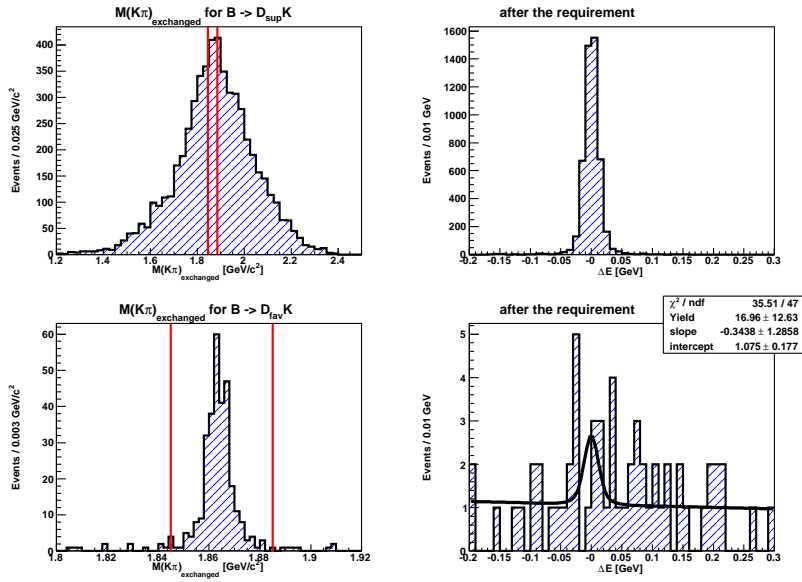
Figure 4.8: The distributions of $M(K\pi)_{\mathrm{exchanged}}$ for the $B^- \to D_{\mathrm{sup}}K^-$ Monte Carlo sample (upper-left) and $B^- \to D_{\mathrm{fav}}K^-$ Monte Carlo sample (lower-left) with $B^- \to D_{\mathrm{sup}}K^-$ selection. The red lines show the range of the veto requirement we use. The right figures show the ΔE distributions after the requirement for each sample. We note that the 30,000 and 1,000,000 events are contained in the Monte Carlo samples for $B^- \to D_{\mathrm{sup}}K^-$ and $B^- \to D_{\mathrm{fav}}K^-$, respectively.
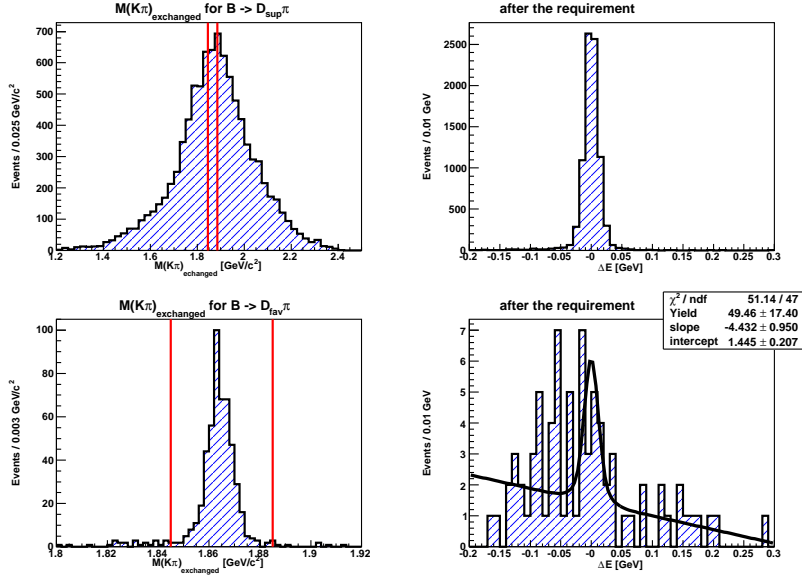
Figure 4.9: The distributions of $M(K\pi)_{\text{exchanged}}$ for the $B^- \to D_{\text{sup}}\pi^-$ Monte Carlo sample (upper-left) and $B^- \to D_{\text{fav}}\pi^-$ Monte Carlo sample (lower-left) with $B^- \to D_{\text{sup}}\pi^-$ selection. The red lines show the range of the veto requirement we use. The right figures show the ΔE distributions after the requirement for each sample. We note that the 30,000 and 1,000,000 events are contained in the Monte Carlo samples for $B^- \to D_{\text{sup}}\pi^-$ and $B^- \to D_{\text{fav}}\pi^-$, respectively.
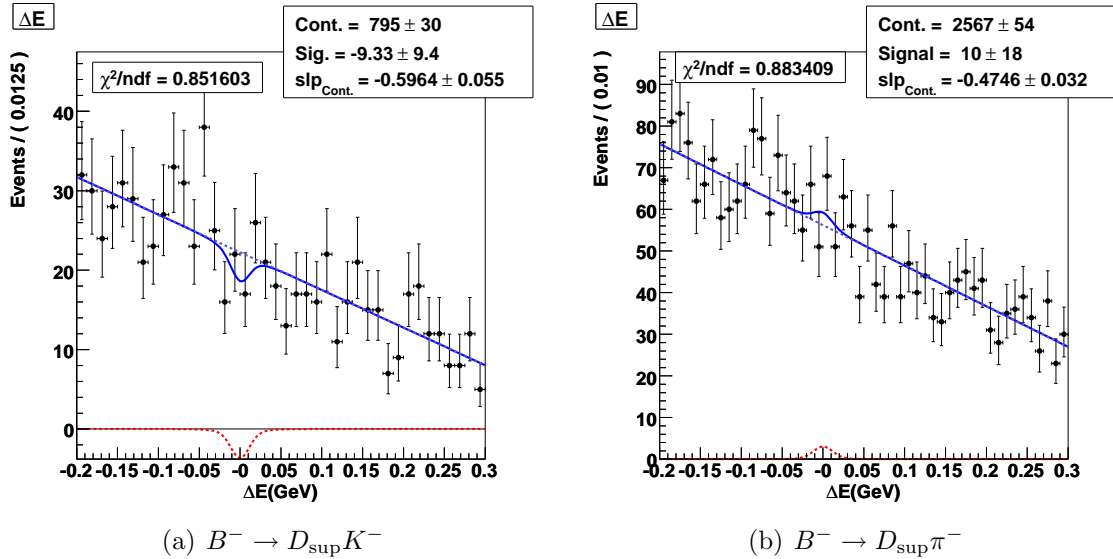

Figure 4.10: The ΔE distributions of the D mass sideband data samples for $B^- \to D_{\text{sup}}K^-$ and $B^- \to D_{\text{sup}}\pi^-$. No significant signals have appeared. The amounts of the samples used here correspond to four times the data samples of signal region.

4.4 Signal Extraction

The signal yields are extracted using extended unbinned maximum likelihood fits to the ΔE distributions of the events which satisfy the selection criteria described in section 4.3. We take the fit to $B^- \to D_{\text{fav}}\pi^-$ at first, and then $B^- \to D_{\text{fav}}K^-$, $B^- \to D_{\text{sup}}\pi^-$, and $B^- \to D_{\text{sup}}K^-$. This order is according to the expected statistics of the signals. In this section, we also provide several checks which are related to the fits.

4.4.1 $B^- \to D_{\text{fav}}\pi^-$

While a large number of events of the decay $B^- \to D_{\text{fav}}\pi^-$ is expected, some backgrounds remain after the selection criteria and make small contributions to the signal yield. Backgrounds from the decays such as $B^- \to D\rho^-$ and $B^- \to D^*\pi^-$ ($B\bar{B}$ background) can populate the negative ΔE region when a pion or a photon is lost. The shape of these backgrounds is modeled with a smoothed function obtained from the $B\bar{B}$ Monte Carlo samples (Figure 4.11), where B and $\bar{B}$ mesons decay generically[4] according to Ref. [7]. The amount of the Monte Carlo samples which are used here corresponds to the luminosity of 1359 fb^{-1}. The continuum background, which is from the two-jet-like $e^+e^- \to q\bar{q}$ ($q = u, d, s, c$) process, populate the entire ΔE region, for which a linear function is used.

Figure 4.12 shows the result of the ΔE fit. To estimate the quality of the fit, a χ^2/ndf (projection χ^2 using the binning of the projection) is used ($\chi^2/ndf = 1.96$). For the signal, we use a sum of two Gaussians, for which all the parameters are floated. We fix the shape parameters for the signal to the fit result obtained here for the other modes, as the validity of which is verified by Monte Carlo study in Figure 4.4.

Efficiency, signal yield and branching ratio are shown in Table 4.1. We have obtained the efficiency from Monte Carlo signal. The calibration of the efficiency for particle identification requirement[5] are then applied to obtain the corrected efficiency $\epsilon_{D_{\text{fav}}\pi^-}$. The branching ratio is calculated from $N_{D_{\text{fav}}\pi^-}/N_{B^-}/\epsilon_{D_{\text{fav}}\pi^-}/\mathcal{B}(D^0 \to K^-\pi^+)$, where $N_{D_{\text{fav}}\pi^-}$ and N_{B^-} show the numbers of signal and total B^-, respectively, and we take $\mathcal{B}(D^0 \to K^-\pi^+)$ from the ref [7]. The error of the branching ratio in Table 4.1 contains only the statistical one.

Mode	$\epsilon_{D_{\text{fav}}\pi^-}$ (%)	Yield	$\mathcal{B}(B^- \to D^0\pi^-)$
$B^- \to D_{\text{fav}}\pi^-$	22.8	27202±176	(4.78±0.03)×10^{-3}

Table 4.1: Efficiency, signal yield and branching ratio. Signal yield is obtained from ΔE fit. The error of the branching ratio contains only the statistical one. The value of the branching ratio in Ref [7] is (4.84±0.15)×10^{-3}.

---

[4]The signal events are taken off here.

[5]Our Monte Carlo sample can't completely actualize the efficiencies of the particle identification requirements. The difference between data and Monte Carlo samples are studied using the decay process of $D^{*-} \to \bar{D}^0\pi^-$ followed by $\bar{D}^0 \to K^+\pi^-$. The factor $\epsilon_{\text{data}}/\epsilon_{\text{MC}}$, where ϵ_{data} and ϵ_{MC} are the efficiencies of the particle identification requirement in data and Monte Carlo samples, respectiely, is estimated for each momentum region of the track.

A check whether we really use whole data samples or not

We have checked the branching ratio dependence on some divided part of the data sample. Figure 4.13 shows the result. While the systematic errors are ignored, the values are stable.
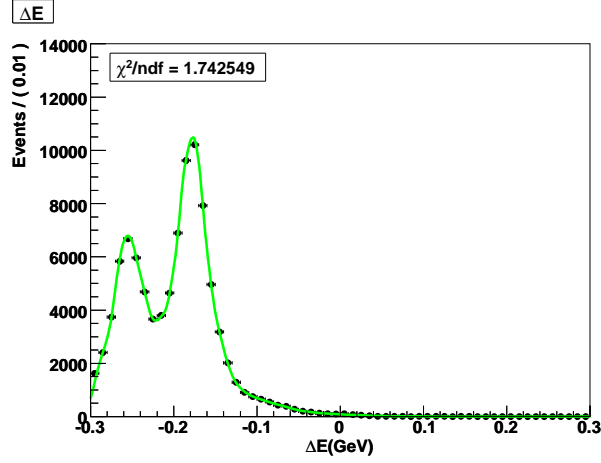

Figure 4.11: The ΔE fit for the Monte Carlo sample with $B^- \rightarrow D_{\mathrm{fav}}\pi^-$ selection, where the signal is taken off. We obtain the smoothed function from this fit.
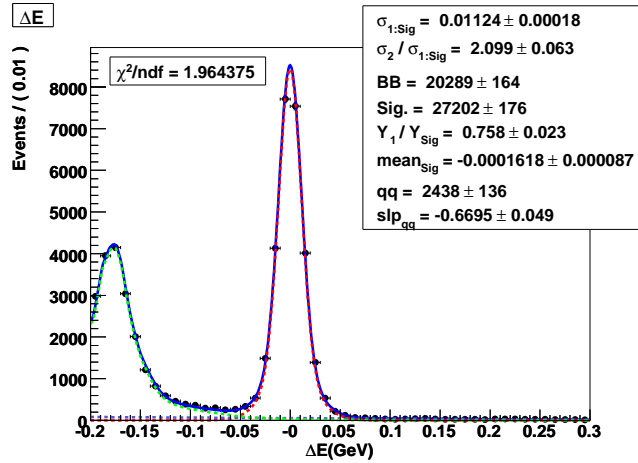

Figure 4.12: ΔE distribution for $B^- \rightarrow D_{\mathrm{fav}}\pi^-$ case.

4.4.2 $B^- \rightarrow D_{\mathrm{fav}}K^-$

For the decay $B^- \rightarrow D_{\mathrm{fav}}K^-$, backgrounds from decays such as $B^- \rightarrow DK^{*-}$ and $B^- \rightarrow D^*K^-$ ($B\bar{B}_{MK^-}$ background) can populate the negative ΔE region, when a pion or a photon is lost. Similarly, those from decays such as $B^- \rightarrow D\rho^-$ and $B^- \rightarrow D^*\pi^-$
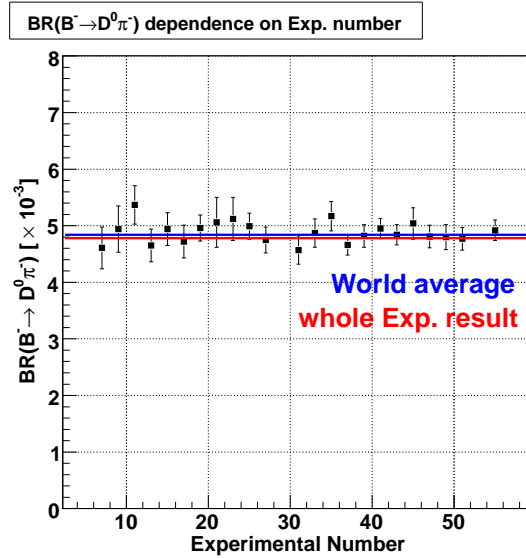
Figure 4.13: The branching ratios of $B^- \to D^0\pi^-$ for some divided parts of the samples, for which we apply experimental numbers.

$(B\bar{B}_{M\pi^-}$ background) can populate the negative ΔE region, if the prompt pion is misidentified as kaon. The feed-across from $B^- \to D_{\text{fav}}K^-$ also appears in the fit, for which the wrong mass assignment makes the position positive. The ΔE distributions of Monte Carlo samples for those backgrounds are shown in Figure 4.14 and 4.15. The strategy for the fit is the following; we consider five components:

- $B^- \to D_{\text{fav}}K^-$ signal (red component): A sum of two Gaussians for which the shape parameters are fixed from the $B^- \to D_{\text{fav}}\pi^-$ fit result are used.

- Feed-across background from $B^- \to D_{\text{fav}}\pi^-$ (magenta): A sum of two asymmetric Gaussians, where the left and the right sides have different widths, is used for this component, because the wrong mass assignment makes the shape asymmetric. We use $B^- \to D_{\text{fav}}\pi^-$ data sample (Figure 4.16) to fix shape parameters, where the kaon mass is assigned to the prompt pion track. Because the shape depends on the particle identification requirement, we float one width and the mean. We mention that the left-side width in the tail is fixed using the Monte Carlo sample of $B^- \to D_{\text{fav}}\pi^-$ (Figure 4.15) since there are many backgrounds over this tail in the Figure 4.16 and it make difficult to fix that parameter.

- $B\bar{B}_{M\pi^-}$ background (green): A smoothed function is used for the $B\bar{B}$ background which has a prompt pion $(B\bar{B}_{M\pi^-})$, for which the shape is fixed from the $B\bar{B}$ Monte Carlo sample with $B^- \to D_{\text{fav}}K^-$ selection (Figure 4.14: green).

- $B\bar{B}_{\text{Others}}$ background (grey): A smoothed function is used for the other $B\bar{B}$ background containing $B\bar{B}_{MK^-}$ background, for which the shape is fixed from the $B\bar{B}$ Monte Carlo sample (Figure 4.14: grey).

- $q\bar{q}$ background (blue dashed): A linear function with free slope is used.

Figure 4.17 shows the result of ΔE fit. We've calculated the branching ratio of $B^- \to D^0 K^-$ and the one of $B^- \to D^0 \pi^-$, which is from $B^- \to D_{\mathrm{fav}} \pi^-$ feed-through events, and shown the values on Table 4.2. For the error, only the statistical ones are applied.
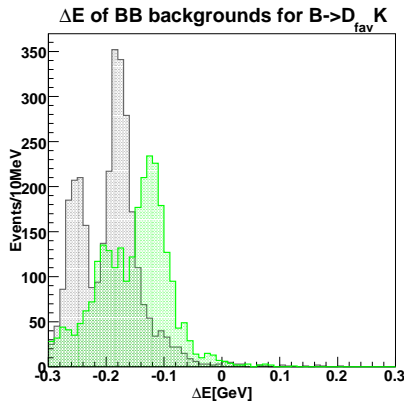

Figure 4.14: ΔE distribution of the Monte Carlo samples for $B\bar{B}$ backgrounds for $B^- \to D_{\mathrm{fav}} K^-$ decay. The green shows $B\bar{B}_{M\pi^-}$ background for which the prompt particles are pion, and the dark line shows the others.

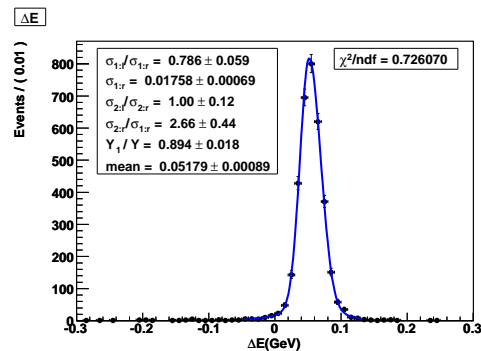Figure 4.15: ΔE fit for the Monte Carlo sample of $B^- \to D_{\mathrm{fav}} \pi^-$, where the kaon mass is assigned to the prompt pion track. The Monte Carlo sample contains 500,000 events. A sum of two asymmetric Gaussian is applied.

Mode	$\epsilon_{D_{\mathrm{fav}}h^-}$ (%)	Yield	$\mathcal{B}(B^- \to D^0 h^-)$
$B^- \to D_{\mathrm{fav}} K^-$	15.1	1220±41	$(3.24\pm0.11)\times10^{-4}$
$B^- \to D_{\mathrm{fav}} \pi^-$	1.33	1506±45	$(4.54\pm0.14)\times10^{-3}$

Table 4.2: Efficiencies, signal yields and branching ratios. We have also obtained $\mathcal{B}(B^- \to D^0 \pi^-)$ from the fitted yield of $B^- \to D_{\mathrm{fav}} \pi^-$ feed-across background. For the error, only the statistical ones are applied.

A check with a two-dimentional fit with $\mathcal{R}$

The $(\Delta E$-$\mathcal{R})$ two-dimentional (2-D) fit is also tried (Figure 4.18 and 4.19). For the signal and $B\bar{B}$ components, we use the shapes of $\mathcal{R}$ obtained from the Monte Carlo samples, and for $q\bar{q}$ background, we use the shape of $\mathcal{R}$ of the data sample in $\Delta E > 0.1$ region, which is dominated by the $q\bar{q}$ component. Table 4.3 shows the obtained branching ratios, for which the error contains only the statistical one. Obtained branching ratios are consistent with the results from the ΔE 1-D fit result (Table 4.2).
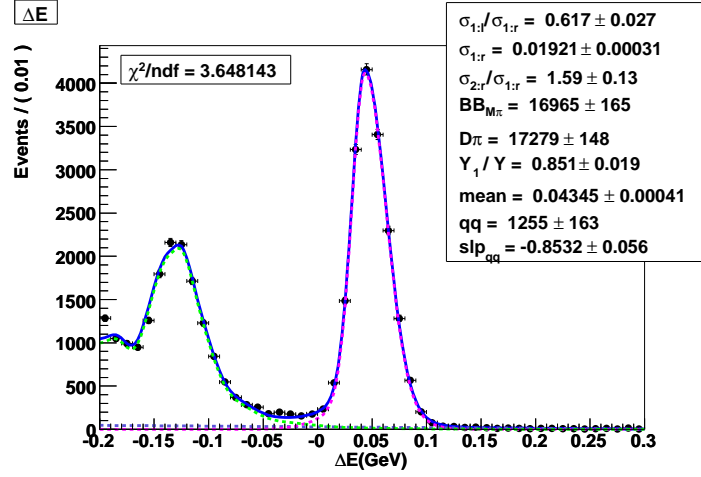
Figure 4.16: ΔE fit for $B^- \to D_{\text{fav}}\pi^-$ data sample, where the kaon mass is assigned to the prompt pion track. A smoothed function for $B\bar{B}_{M\pi^-}$ and a sum of two asymmetric Gaussians is used.
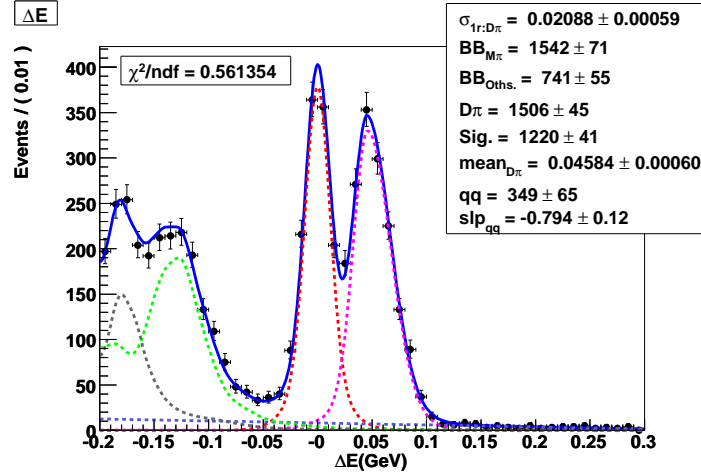

Figure 4.17: ΔE fit for $B^- \to D_{\text{fav}}K^-$. The difference of the ratios of $B\bar{B}_{M\pi^-}$ and $B\bar{B}_{\text{Others}}$ yields between data (this figure) and Monte Carlo (Figure 4.14) is caused by the difference of the efficiency of particle identification requirement for prompt pion in data and Monte Carlo samples.

Mode	$\epsilon_{D_{\text{fav}}h^-}$ (%)	Yield	$\mathcal{B}(B^- \to D^0 h^-)$
$B^- \to D_{\text{fav}}K^-$ (2-D)	32.5	2780±63	$(3.43\pm0.08)\times10^{-4}$
$B^- \to D_{\text{fav}}\pi^-$ (2-D)	3.24	3716±73	$(4.59\pm0.09)\times10^{-3}$

Table 4.3: Efficiencies, signal yields and branching ratios from the (ΔE-$\mathcal{R}$) 2-D fit. The error contains only the statistical one.
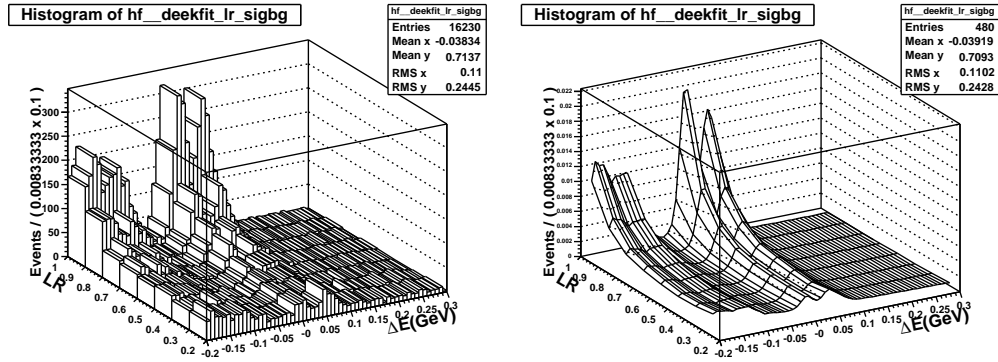
Figure 4.18: (ΔE-$\mathcal{R}$) 2-D fit for $B^- \to D_{\text{fav}}K^-$. The left is the data and the right is the fitted function.

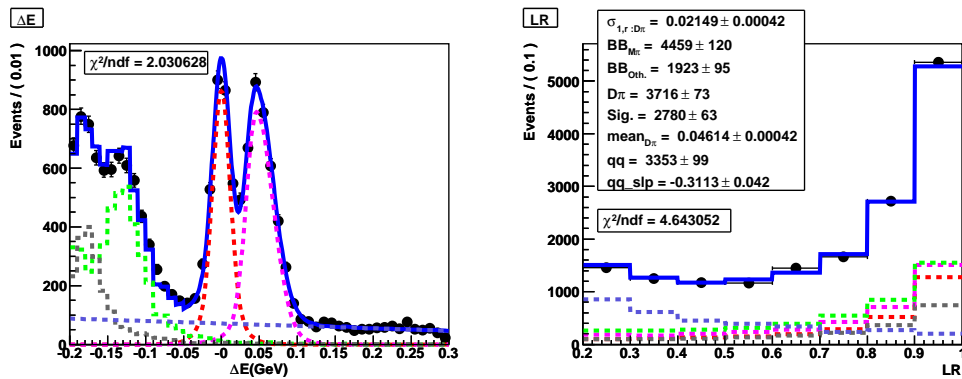Figure 4.19: Projections of the (ΔE-$\mathcal{R}$) 2-D fit for $B^- \to D_{\text{fav}}K^-$.

4.4.3 $B^- \to D_{\text{sup}}\pi^-$

For $B^- \to D_{\text{sup}}\pi^-$, we consider three components as in the case for $B^- \to D_{\text{fav}}\pi^-$. We use a smoothed function (Figure 4.20) obtained using Monte Carlo sample for $B\bar{B}$ background, a linear function for $q\bar{q}$ background, and a sum of two Gaussian, for which the shape parameters are fixed to the result of $B^- \to D_{\text{fav}}\pi^-$, for the signal. Figure 4.21 and Table 4.4 show the result. The error of the branching ration contains only the statistical one.
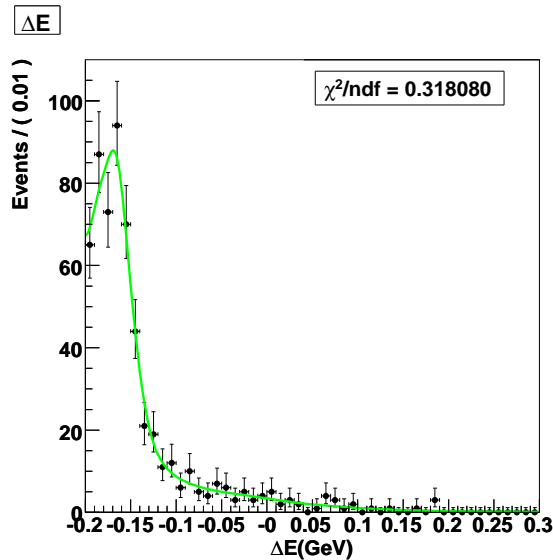

Figure 4.20: ΔE fit for the Monte Carlo sample of $B\bar{B}$ background for $B^- \to D_{\text{sup}}\pi^-$.

Mode	$\epsilon_{D_{\text{sup}}\pi^-}$ (%)	Yield	$\mathcal{B}(B^- \to D^0 h^-)$
$B \to D_{\text{sup}}\pi$	23.1	$(99.8-6.0)\pm15.0$	$(4.26\pm0.68)\times10^{-3}$

Table 4.4: Efficiencies, signal yields and branchiung ratios for $B^- \to D_{\text{sup}}\pi^-$ analysis. The expected yield of the peaking background, which is studied in the section 4.3.5, is subtracted. The error contains only the statistical one.

A check using an alternative shape for $B\bar{B}$ background

We also try to use an alternative shape, a sum of two asymmetric Gaussians, for the $B\bar{B}$ background component, since the Monte Carlo sample used for fixing the shape of the smoothed function above, is not contains all of the background from $B\bar{B}$[6]. Figure 4.21 shows the result. In this approach, some part of the contribution of $B\bar{B}$ background seems to be included in the linear function. The signal yield is consistent with the result of the previous fit.

---

[6]The $B\bar{B}$ background for $B^- \to D_{\text{sup}}\pi^-$ seems to contain suppressed decays for which we don't know the branching ratios.
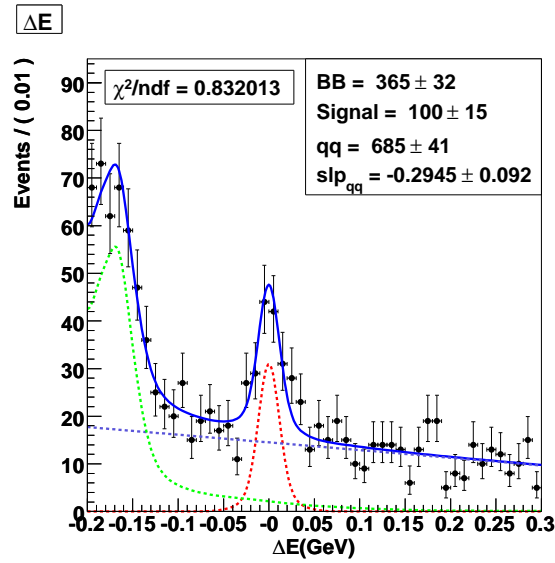
Figure 4.21: ΔE fit for $B^- \to D_{\mathrm{sup}}\pi^-$ case.
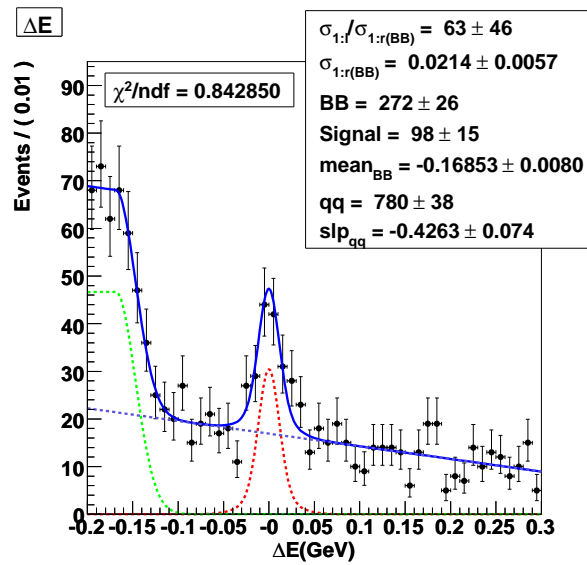
Figure 4.22: An alternative ΔE fit for $B^- \to D_{\mathrm{sup}}\pi^-$. A sum of two asymmetric Gaussians is used for $B\bar{B}$ background.

4.4.4 $B^- \to D_{\mathrm{sup}}K^-$

The strategy for the fit to $B^- \to D_{\mathrm{sup}}K^-$ is the following. We consider five components as in the case for $B^- \to D_{\mathrm{fav}}K^-$.

- $B^- \to D_{\mathrm{sup}}K^-$ signal (red component): A sum of two Gaussians for which the shape parameters are fixed from the $B^- \to D_{\mathrm{fav}}\pi^-$ fit result are used.

- Feed-across background from $B^- \to D_{\mathrm{sup}}\pi^-$ (magenta): A sum of two asymmetric Gaussians is used, where the shape parameters are fixed from the fit to $B^- \to D_{\mathrm{fav}}K^-$ (Figure 4.17) and the yield is fixed from the efficiency of $B^- \to D_{\mathrm{fav}}\pi^-$ in the analysis for $B^- \to D_{\mathrm{fav}}K^-$ and N_{B^-}.

- $B\bar{B}_{M\pi^-}$ background (green): An asymmetric Gaussian is used for the $B\bar{B}$ background which has a daughter prompt pion. All of the parameters are fixed from the fit for the data sample of $B^- \to D_{\mathrm{sup}}\pi^-$, where the kaon mass is assigned to the prompt pion: Figure 4.23. This function doesn't cover all of the $B\bar{B}_{M\pi^-}$ component, and the tail is included in the linear function described below.

- $B\bar{B}_{MK^-}$ background (grey): A smoothed function, for which the shape is the same as for $B^- \to D_{\mathrm{fav}}K^-$. We don't know many about this components, since this contains suppressed decays for which we don't know the branching ratios. The smoothed function and the linear function below seems to cover the $B\bar{B}_{MK^-}$ component.

- The other $B\bar{B}$ and $q\bar{q}$ backgrounds (blue dashed): A linear function with free slope is used for some part of $B\bar{B}$[7] and $q\bar{q}$ background.

Figure 4.24 and Table 4.5 shows the result.

The statistical significance, which is defined as $\sqrt{-2\ln(\mathcal{L}_0/\mathcal{L}_{\mathrm{max}})}$ where $\mathcal{L}_{\mathrm{max}}$ is the maximum likelihood in the ΔE fit and $\mathcal{L}_0$ is the likelihood when the signal yield is constrained to be zero, is 1.5σ.

Mode	$\epsilon_{D_{\mathrm{sup}}K^-}$ (%)	Yield
$B^- \to D_{\mathrm{sup}}K^-$	15.4	$(10.1-0.22-0.17)\pm7.4$

Table 4.5: Efficiencies and signal yields for $B^- \to D_{\mathrm{sup}}K^-$ analysis.

---

[7]There seems to be the backgrounds from $B\bar{B}$ in the whole part of ΔE (Appendix A).
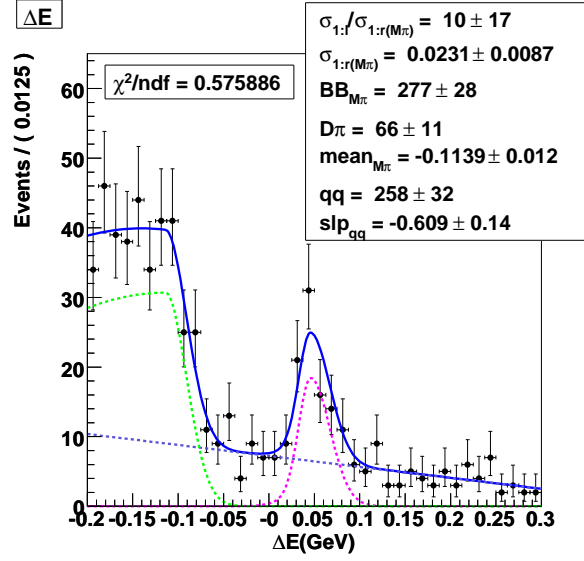
Figure 4.23: ΔE fit for $B^- \to D_{\text{sup}}\pi^-$ data sample, where the kaon mass is assigned to the prompt pion. An aymmetric Gaussian is used for some part of $B\bar{B}_{M\pi^-}$. The other part of $B\bar{B}_{M\pi^-}$ is contained in the linear function. The linear function also includes $q\bar{q}$ background.
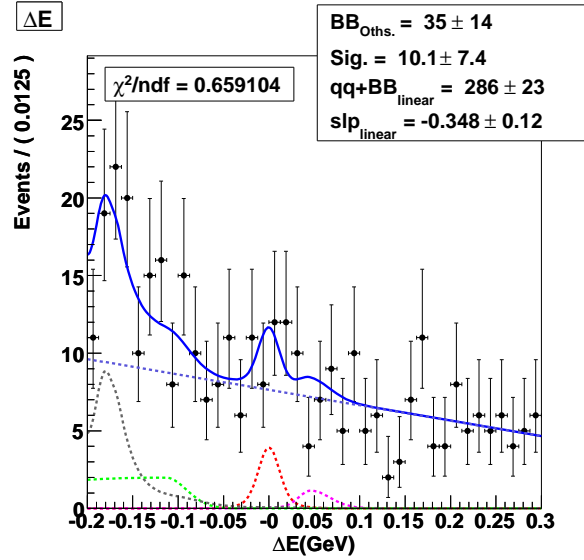

Figure 4.24: ΔE fit for $B^- \to D_{\text{sup}}K^-$. Free parameters are only three yields and a slope of the linear function.

Chapter 5

Results

We determine several values in this analysis. Table 5.1 shows the summary of the detection efficiencies and the fitted yields. The errors of the efficiencies are dominated by the Monte Carlo statistics and the uncertainties in the efficiencies of particle identification requirements. For the yields, we subtracted peaking backgrounds according to the studies in section 4.3.5. The errors of the yields contain only statistical one in the ΔE fits.

Mode	Efficiency (%)	Yield	Significance
$B^- \to D_{\mathrm{sup}} K^-$	15.4 ± 0.3	$9.7^{+7.7}_{-7.0}$	1.5σ
$B^- \to D_{\mathrm{sup}} \pi^-$	23.1 ± 0.4	$93.8^{+15.3}_{-14.8}$	8.4σ
$B^- \to D_{\mathrm{fav}} K^-$	15.1 ± 0.3	1220^{+41}_{-40}	63σ
$B^- \to D_{\mathrm{fav}} \pi^-$	22.8 ± 0.4	27202^{+177}_{-176}	360σ

Table 5.1: Summary table of the detection efficiencies and the signal yields with statistical significances which are the values $\sqrt{-2\ln(\mathcal{L}_0/\mathcal{L}_{\max})}$ (see the section 4.4.4) in the ΔE fits.

5.1 Ratio of branching fraction R_{Dh}

We define the ratio

$$R_{Dh} \equiv \frac{\mathcal{B}(B^- \to D_{\mathrm{sup}} h^-)}{\mathcal{B}(B^- \to D_{\mathrm{fav}} h^-)} = \frac{N_{D_{\mathrm{sup}} h^-}/\epsilon_{D_{\mathrm{sup}} h^-}}{N_{D_{\mathrm{fav}} h^-}/\epsilon_{D_{\mathrm{fav}} h^-}}, \tag{5.1}$$

where $N_{D_{\mathrm{sup}} h^-}$ ($N_{D_{\mathrm{fav}} h^-}$) and $\epsilon_{D_{\mathrm{sup}} h^-}$ ($\epsilon_{D_{\mathrm{fav}} h^-}$) are the number of signal events and the reconstruction efficiency for the decay $B^- \to D_{\mathrm{sup}} h^-$ ($B^- \to D_{\mathrm{fav}} h^-$), which are given in Table 5.1. We obtain

$$R_{DK} = [8.0^{+6.3}_{-5.7}(stat)^{+2.0}_{-2.8}(sys)] \times 10^{-3}, \tag{5.2}$$
$$R_{D\pi} = [3.40^{+0.56}_{-0.54}(stat)^{+0.13}_{-0.21}(sys)] \times 10^{-3}, \tag{5.3}$$

where the systematic errors are subdivided as follows: The systematic error due to the yield extraction is estimated (Table 5.2) to be 26% (3.1%) for R_{DK} ($R_{D\pi}$), where the

uncertainty due to the shapes of the signal and the $q\bar{q}$ background is obtained by varying the shape parameters by $\pm 1\sigma$, and that due to the shapes of the $B\bar{B}$ backgrounds is estimated by fitting the ΔE distribution in the region -0.05 GeV $< \Delta E < 0.15$ GeV ignoring the $B\bar{B}$ background contributions. The uncertainty due to the peaking backgrounds has been described in the section 4.3.5, and the corresponding systematic error in R_{DK} $(R_{D\pi})$ is estimated to be 25% (4.8%) which is only for the negative side. The Monte Carlo statistics and the uncertainties in the efficiencies of particle identification requirements dominate the systematic error in detection efficiency, which is estimated to be 2.7% (2.5%) for R_{DK} $(R_{D\pi})$. The total systematic error is the sum in quadrature of the above errors.

Source	Systematic error(%)			
	$B^- \to D_{\text{sup}}K^-$	$B^- \to D_{\text{fav}}K^-$	$B^- \to D_{\text{sup}}\pi^-$	$B^- \to D_{\text{fav}}\pi^-$
$B\bar{B}$ background	± 25.5	± 2.3	± 1.8	± 0.48
$q\bar{q}$ background	$\uparrow$	± 0.0	± 0.5	± 0.01
Signal shape	± 4.1	± 1.1	± 2.5	± 0.07
Feed-across	± 1.0	± 1.7	-	-

Table 5.2: Systematic uncertainties of yield extractions. For $B^- \to D_{\text{sup}}K^-$, the errors due to the components for $B\bar{B}$ and $q\bar{q}$ backgrounds are mixed because the linear function in $B^- \to D_{\text{sup}}K^-$ fit has a role for some part of $B\bar{B}$ backgrounds.

Since the signal for $B^- \to D_{\text{sup}}K^-$ is not statistically significant, we set an upper limit at the 90% confidence level (C.L.) of

$$R_{DK} < 1.8 \times 10^{-2}, \tag{5.4}$$

which is estimated as follows: We take the likelihood function of the number of signal obtained in the ΔE fit, convolute with a Gaussian which represents the systematic error, and normalize the area of the resulting function in the physical region of positive branching fraction to define the 90% C.L. upper limit.

Using the values of R_{Dh} obtained above, we determine the branching fractions for $B^- \to D_{\text{sup}}h^-$ using

$$\mathcal{B}(B^- \to D_{\text{sup}}h^-) = \mathcal{B}(B^- \to D_{\text{fav}}h^-) \times R_{Dh}. \tag{5.5}$$

The results are given in Table 5.3. An additional uncertainty arises because of the error in the branching fraction of $B^- \to D_{\text{fav}}h^-$, which is taken from Ref. [7]. For the $B^- \to D_{\text{sup}}K^-$ branching fraction, we set an upper limit at the 90% C.L. of

$$\mathcal{B}(B^- \to D_{\text{sup}}K^-) < 2.8 \times 10^{-7}. \tag{5.6}$$

Our branching fraction for $B^- \to D_{\text{sup}}\pi^-$ is consistent with the value expected from the branching fractions of B and D in Ref. [7].

The ratio R_{DK} is related to ϕ_3 by

$$R_{DK} = r_B^2 + r_D^2 + 2r_B r_D \cos\phi_3 \cos\delta \tag{5.7}$$

Table 5.3: Branching fraction for $B^- \to D_{\mathrm{sup}}h^-$. The first two errors on the measured branching fractions are statistical and systematic, respectively, and the third is due to the uncertainty in the $B^- \to D_{\mathrm{fav}}h^-$ branching fraction used for normalization. For $B^- \to D_{\mathrm{sup}}\pi^-$, we calculate the expectation of branching fraction by $\mathcal{B}(B^- \to D^0\pi^-) \times \mathcal{B}(D^0 \to K^+\pi^-)$ [7].

Mode	Expetation of branching fraction from [7]	Measured branching fraction	Upper limit (90% C.L.)
$B^- \to D_{\mathrm{sup}}K^-$	$\cdots$	$(1.2^{+1.0+0.3}_{-0.9-0.4} \pm 0.1) \times 10^{-7}$	2.8×10^{-7}
$B^- \to D_{\mathrm{sup}}\pi^-$	$(7.02 \pm 0.29) \times 10^{-7}$	$(6.29^{+1.04+0.24}_{-1.00-0.39} \pm 0.24) \times 10^{-7}$	$\cdots$

where [23]

$$r_B \equiv \left| \frac{A(B^- \to \bar{D}^0 K^-)}{A(B^- \to D^0 K^-)} \right| , \quad \delta \equiv \delta_B + \delta_D , \tag{5.8}$$

$$r_D \equiv \left| \frac{A(D^0 \to K^+\pi^-)}{A(D^0 \to K^-\pi^+)} \right| = 0.0574^{+0.0012}_{-0.0010}, \tag{5.9}$$

and δ_B and δ_D are the strong phase differences between the two B and D decay amplitudes, respectively. Using the above result, we obtain a limit on r_B. The least restrictive upper limit at 90% C.L. is obtained by taking $+2\sigma$ variation on r_D and assuming $\cos\phi_3 \cos\delta = -1$, and is found to be (Figure 5.1)

$$r_B < 0.19. \tag{5.10}$$

5.2 CP asymmetry $\mathcal{A}_{Dh}$

We measure a partial rate asymmetry $\mathcal{A}_{Dh}$ in $B^\mp \to D_{\mathrm{sup}}h^\mp$ decay by fitting the B^- and B^+ yields separately for each mode, where $\mathcal{A}_{Dh}$ is determined as

$$\mathcal{A}_{Dh} \equiv \frac{\mathcal{B}(B^- \to D_{\mathrm{sup}}h^-) - \mathcal{B}(B^+ \to D_{\mathrm{sup}}h^+)}{\mathcal{B}(B^- \to D_{\mathrm{sup}}h^-) + \mathcal{B}(B^+ \to D_{\mathrm{sup}}h^+)} \quad (h = K, \pi). \tag{5.11}$$

The peaking backgrounds are subtracted assuming no CP asymmetry[1]. The results are shown in Table 5.4 and Figure 5.2 and 5.3, where the slopes for the linear functions are fixed using the results in Figure 4.21 and 4.24. For $B^\mp \to D_{\mathrm{sup}}K^\mp$, the yields of the feed-across background from $B^- \to D_{\mathrm{sup}}\pi^-$ and of the $B\bar{B}_{M\pi^-}$ background are fixed to the halves to the results in Figure 4.24. We find

$$\mathcal{A}_{DK} = -0.13^{+0.97}_{-0.88}(stat) \pm 0.26(sys), \tag{5.12}$$

$$\mathcal{A}_{D\pi} = -0.023 \pm 0.218(stat) \pm 0.071(sys), \tag{5.13}$$

---

[1] An assumption of 30% CP asymmetries in the peaking backgrounds would lead to shifts of 0.01 in $\mathcal{A}_{DK}$ and 0.019 in $\mathcal{A}_{D\pi}$.
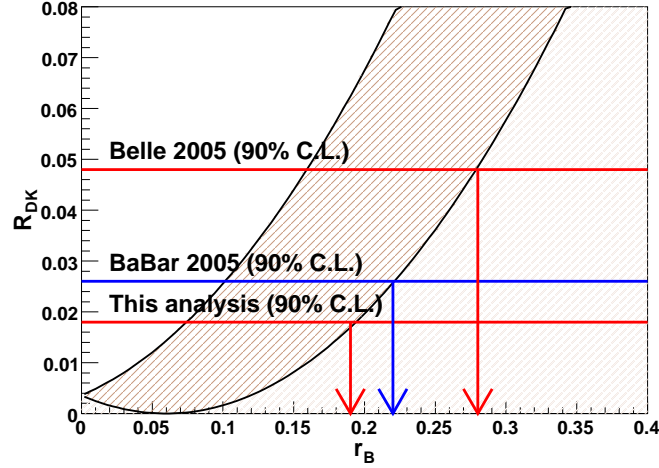
Figure 5.1: The dependence of R_{DK} on r_B, together with our limit and the previous limits. Allowed region, shown with hatched lines, is assumed as $\pm 2\sigma$ variation on r_D and any values of ϕ_3 and δ.

where the systematic errors are dominated by the uncertainties in the yield extractions, for the estimation of which we use the same methods as in the section 5.1. Possible biases due to the asymmetry of the detector is estimated using the $B^- \to D_{\mathrm{fav}}\pi^-$ control sample, and the uncertainty in the particle identification requirement for prompt kaon is studied in Ref. [24], both of which are found to be negligible. The total systematic errors are combined as the quadratic sum of those uncertainties (Table 5.5). The measured partial rate asymmetries $\mathcal{A}_{Dh}$ are consistent with zero within large errors.

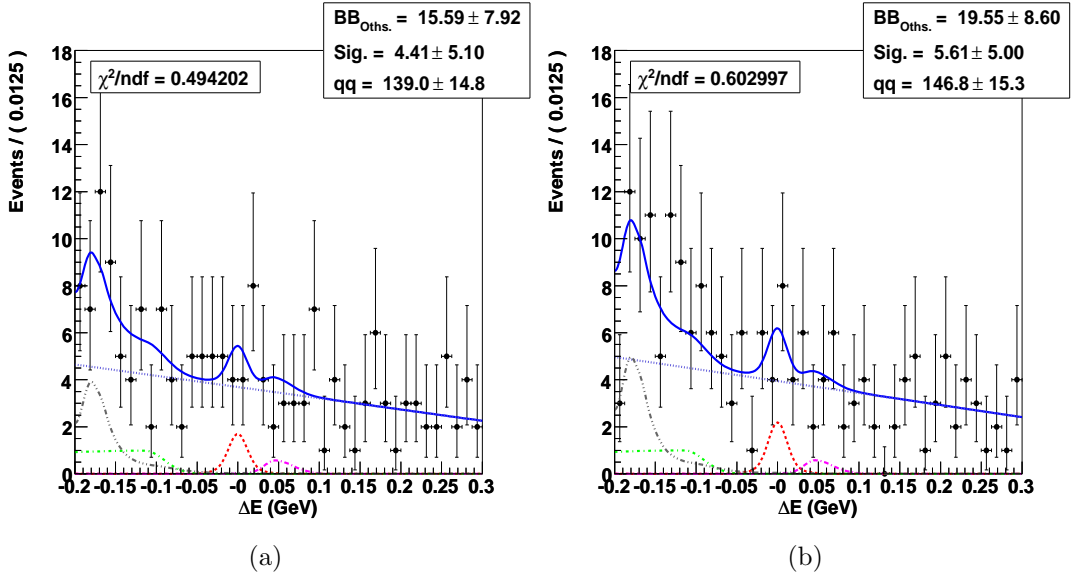| Mode	$N(B^-)$	$N(B^+)$	$\mathcal{A}_{Dh}$
$B^{\mp} \to D_{\mathrm{sup}}K^{\mp}$	$4.2^{+5.5}_{-4.7}$	$5.4^{+5.4}_{-4.6}$	$-0.13^{+0.97}_{-0.88} \pm 0.26$
$B^{\mp} \to D_{\mathrm{sup}}\pi^{\mp}$	$45.7^{+10.7}_{-10.0}$	$47.9^{+10.6}_{-9.8}$	$-0.023 \pm 0.218 \pm 0.071$

Table 5.4: Signal yields and the asymmetries. Yields are the values after subtracting peaking backgrounds.

5.3   ADS fit

A constraint on ϕ_3 is determined with the result of $B^- \to D_{CP(\pm)}K^-$, where $D_{CP(\pm)}$ denote the CP eigenstates $D_{CP(\pm)} = (D^0 \pm \bar{D}^0)/\sqrt{2}$. To give a constraint, we use the

Source	Sys. on $\mathcal{A}_{DK}$	Sys. on $\mathcal{A}_{D\pi}$
Yield extraction	± 0.26	± 0.070
Intrinsic detector charge asym	± 0.009	± 0.009
PID efficiency of prompt kaons	± 0.006	-
Total	± 0.26	± 0.070

Table 5.5: Sources of systematic uncertainties for the asymmetry calculation.

Figure 5.2: ΔE fits for $B^- \to D_{\sup} K^-$ (a) and $B^+ \to D_{\sup} K^+$ (b).
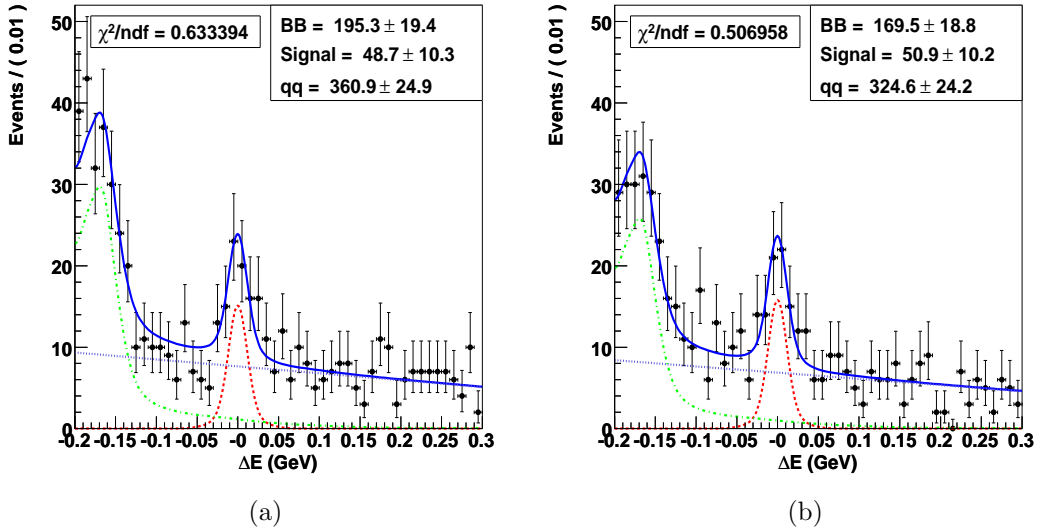
Figure 5.3: ΔE fits for $B^- \to D_{\sup} \pi^-$ (a) and $B^+ \to D_{\sup} \pi^+$ (b).

parameters below[2]:

$$
\begin{aligned}
R_{DK}^{\pm} &\equiv \frac{\mathcal{B}(B^{\pm} \to D_{\mathrm{sup}}K^{\pm})}{(\mathcal{B}(B^- \to D_{\mathrm{fav}}K^-) + \mathcal{B}(B^+ \to D_{\mathrm{fav}}K^+))/2} \\
&= r_B^2 + r_D^2 + 2r_B r_D \cos(\delta \pm \phi_3) & (5.14) \\
\mathcal{A}_{CP(\pm)} &\equiv \frac{\mathcal{B}(B^- \to D_{CP(\pm)}K^-) - \mathcal{B}(B^+ \to D_{CP(\pm)}K^+)}{\mathcal{B}(B^- \to D_{CP(\pm)}K^-) + \mathcal{B}(B^+ \to D_{CP(\pm)}K^+)} \\
&= \frac{2r_B \sin \delta'_{CP} \sin \phi_3}{1 + r_B^2 + 2r_B \cos \delta'_{CP} \cos \phi_3} & (5.15) \\
R_{CP(\pm)} &\equiv \frac{\mathcal{B}(B^- \to D_{CP(\pm)}K^-) + \mathcal{B}(B^+ \to D_{CP(\pm)}K^+)}{\mathcal{B}(B^- \to D^0 K^-) + \mathcal{B}(B^+ \to \bar{D}^0 K^+)} \\
&= 1 + r_B^2 + 2r_B \cos \delta'_{CP} \cos \phi_3 & (5.16) \\
\delta'_{CP} &\equiv \begin{cases} \delta_{CP} & (\text{for } D_{CP(+)}) \\ \delta_{CP} + \pi & (\text{for } D_{CP(-)}). \end{cases} & (5.17)
\end{aligned}
$$

The input values used here are

$$
\begin{aligned}
R_{DK}^+ &= (8.9^{+8.9}_{-7.5}(stat) \pm 2.9(sys)) \times 10^{-3} & (5.18) \\
R_{DK}^- &= (6.9^{+9.0}_{-7.7}(stat) \pm 3.9(sys)) \times 10^{-3} & (5.19) \\
\mathcal{A}_{CP(+)} &= 0.22 \pm 0.14 & (5.20) \\
\mathcal{A}_{CP(-)} &= -0.09 \pm 0.10 & (5.21) \\
R_{CP(+)} &= 0.90 \pm 0.13 & (5.22) \\
R_{CP(-)} &= 0.87 \pm 0.11, & (5.23)
\end{aligned}
$$

where R_{DK}^+ and R_{DK}^- are estimated using the results in Figure 5.2, and the others are taken from Ref. [7].

We have six equations and four unknown parameters, which are ϕ_3, r_B, δ, and δ_{CP}. We calculate $\chi^2(\phi_3, r_B, \delta, \delta_{CP})$ defined as

$$
\chi^2(\phi_3, r_B, \delta, \delta_{CP}) = \sum_i \frac{(\mathcal{O}_{\mathrm{measured}}^i - \mathcal{O}^i(\phi_3, r_B, \delta, \delta_{CP}))^2}{\sigma_{\mathcal{O}^i}^2}, \tag{5.24}
$$

where $\mathcal{O}_{\mathrm{measured}}^i$ are the measured values given in Eq. (5.18)-(5.23), $\mathcal{O}^i(\phi_3, r_B, \delta, \delta_{CP})$ is the values in Eq. (5.14)-(5.16) as functions of ϕ_3, r_B, δ, and δ_{CP}, and $\sigma_{\mathcal{O}^i}$ is the experimental errors in Eq. (5.18)-(5.23). Then, we calculate the probability on ϕ_3 and r_B as

$$
P(\phi_3, r_B) = \iint \mathcal{L}(\phi_3, r_B, \delta, \delta_{CP}) \, d\delta \, d\delta_{CP}, \tag{5.25}
$$

where the likelihood $\mathcal{L}$ is given by

$$
\mathcal{L}(\phi_3, r_B, \delta, \delta_{CP}) = e^{-\frac{1}{2}\chi^2(\phi_3, r_B, \delta, \delta_{CP})}. \tag{5.26}
$$

The result is shown in Figure 5.4. We set a 90% C.L. upper limit on r_B as $r_B < 0.09$, while the constraint on ϕ_3 is not strong.

---

[2]We imply the D decays for 'D_{sup}' and 'D_{fav}', while we don't contain decays of D for '$D_{CP(\pm)}$', 'D^0', and '$\bar{D}^0$'.
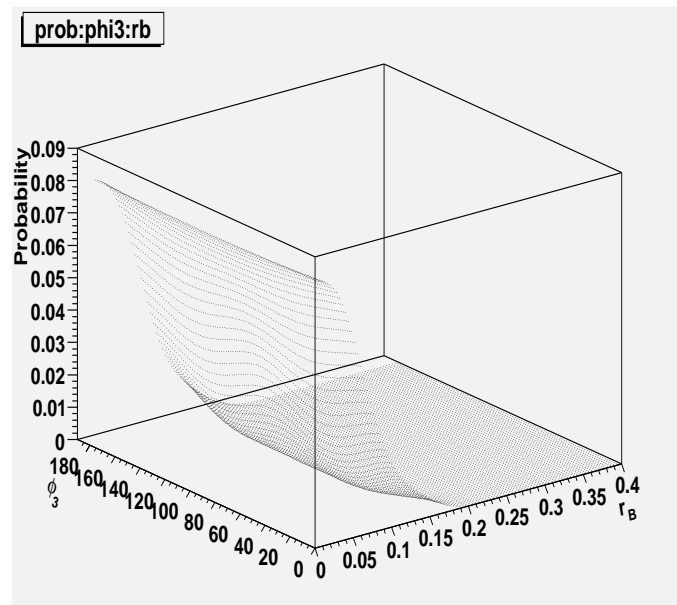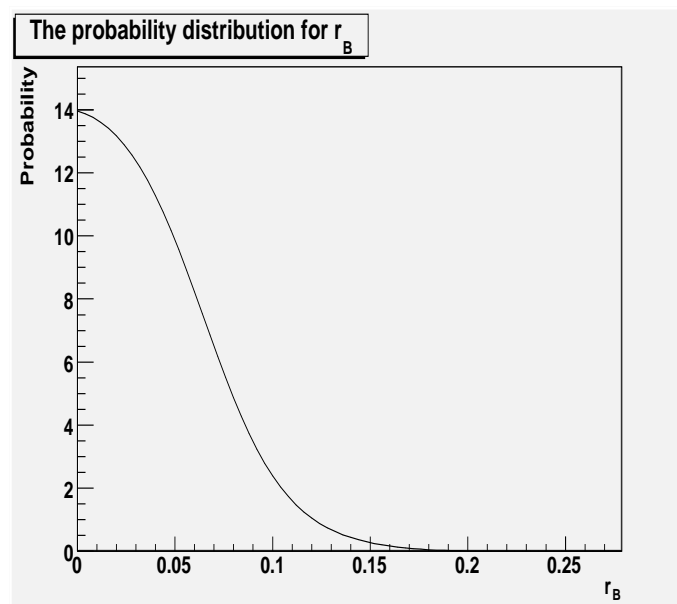
(a) Probability distribution on ϕ_3 and r_B.

(b) Probability distribution on r_B.

Figure 5.4: Probability distributions.

5.4   Another result

We also report $\mathcal{B}(B^- \to D^0 K^-)/\mathcal{B}(B^- \to D^0 \pi^-)$ from the analysis of $B^- \to D_{\text{fav}} K^-$ and $B^- \to D_{\text{fav}} \pi^-$. Our value is

$$\frac{\mathcal{B}(B^- \to D^0 K^-)}{\mathcal{B}(B^- \to D^0 \pi^-)} = \frac{N_{D_{\text{fav}} K^-}}{N_{D_{\text{fav}} \pi^-}} \frac{\epsilon_{D_{\text{fav}} \pi^-}}{\epsilon_{D_{\text{fav}} K^-}} \tag{5.27}$$

$$= (6.77 \pm 0.23(stat) \pm 0.30(sys)) \times 10^{-2}. \tag{5.28}$$

The systematic errors are due to the uncertainty in the yield extractions (3.1%, Table 5.2) and the one of efficiency estimations (1.9%). The latter is the quadratic sum of the efficiency's error given in Table 5.3 and the uncertainty due to the difference of the particle identification requirements for prompt particles in $B^- \to D_{\text{fav}} K^-$ and $B^- \to D_{\text{fav}} \pi^-$ analyses, which is studied in Appendix B.1. The uncertainty due to the difference of $\mathcal{R}$ requirements can be ignored (Appendix B.2). Assuming the value $\mathcal{B}(B^- \to D^0 \pi^-)=(4.84 \pm 0.15) \times 10^{-3}$ in Ref. [7], $\mathcal{B}(B^- \to D^0 K^-)$ is obtained as

$$\mathcal{B}(B^- \to D^0 K^-) = (3.28 \pm 0.11(stat) \pm 0.15(sys) \pm 0.10) \times 10^{-4}, \tag{5.29}$$

where the third error comes from the error of $\mathcal{B}(B^- \to D^0 \pi^-)$. We note that the value of $\mathcal{B}(B^- \to D^0 K^-)$ in Ref. [7] is $(4.02 \pm 0.21) \times 10^{-4}$.

Chapter 6

Conclusion

In summary, using 657×10^6 $B\bar{B}$ pairs collected with the Belle detector, we report studies of the suppressed decays $B^- \rightarrow D_{\mathrm{sup}}h^-$ ($h = K, \pi$). No significant signal is observed for $B^- \rightarrow D_{\mathrm{sup}}K^-$ and we set a 90% C.L. upper limit on the ratio of B decay amplitudes as $r_B < 0.19$. This result is consistent with previous searches [25, 26], and with the measurement of r_B in the decay $B^- \rightarrow [K_S^0 \pi^+ \pi^-]_D K^-$ [27]. We have also performed ADS fit and set a 90% C.L. upper limit of $r_B < 0.09$, while the constraint on ϕ_3 is not strong. For the reference decay $B^- \rightarrow D_{\mathrm{sup}}\pi^-$, we observe a signal with a statistical significance of 8.4σ and the size of the signal is consistent with the expectation. Additionally, the charge asymmetry of $B^{\mp} \rightarrow D_{\mathrm{sup}}h^{\mp}$ and the ratio $\mathcal{B}(B^- \rightarrow D^0 K^-)/\mathcal{B}(B^- \rightarrow D^0 \pi^-)$ are reported, which are both consistent with the predictions.

Appendix A

Background study with Dalitz distribution

Figure A.1 shows the Dalitz distributions and the ΔE distributions for the data samples of $B^- \rightarrow D_{\mathrm{sup}} h^-$ candidate events, for which a ΔE cut of -0.2 GeV $< \Delta E < 0.3$ GeV and all the other cuts described in section 4.3 are applied. There are some structures in the plots.

We tried to check the contributions using MC samples containing 628 $B\bar{B}$ pairs. Figure A.2 (a) shows the Dalitz and ΔE distributions for $B\bar{B}$ generic MC samples with $B^- \rightarrow D_{\mathrm{sup}} K^-$ selection. In the Figure A.2 (b), those distributions for several decay modes are shown. There are the decays $B^- \rightarrow D^0 \pi^-$, $B^- \rightarrow D^{*0} \pi^-$, $B^- \rightarrow D^0 \rho^-$, $B^- \rightarrow J/\psi K^-$, $\bar{B}^0 \rightarrow D^+ \pi^-$, and so on, which are thought to be distributed also in the data sample. The decays which have not been included in the $B\bar{B}$ MC, like $B^- \rightarrow K^{*0} K^-$ and $B^- \rightarrow \phi \pi^-$, may also appear in the data sample. However, those decays have not so much effects on our analysis. Additionally, the Dalitz and ΔE distributions for $B\bar{B}$ generic MC samples with $B^- \rightarrow D_{\mathrm{sup}} \pi^-$ selection are shown in Figure A.3. Similar decay modes appear with different distributions because of the differences of the mass asignments for the prompt particle candidates. Because the ΔE distributions depend on the decay modes, and several decays appear in the several parts of the Dalitz plane, to use the events in the region close to signal region is suitable for the estimation of the backgrounds which contribute to our signal yields. Figure A.4 shows the ΔE distributions for some D mass sideband slices of the data samples for $B^- \rightarrow D_{\mathrm{sup}} h^-$. The sum of the region 1 and region 2 in the Figure A.4, which is the same region as used in section 4.3, seems to be good region for the estimation of peaking backgrounds.

A.1   A possibility to get better $S/\sqrt{S+B}$

Because the region $M(K^+ K^-)^2 < 6$ seems to have many backgrounds, the requirement of $M(K^+ K^-)^2 > 6$ may increase the value $S/\sqrt{S+B}$. Using MC, we have estimated the value $S/\sqrt{S+B}$ for $B^- \rightarrow D_{\mathrm{sup}} K^-$ as follows:

- $1.6 \sim 2.9$ without $M(K^+ K^-)$ requirement, and

- $1.8 \sim 3.0$ with the requirement of $M(K^+K^-)^2 < 6$,

where the signal yield is assumed to be $10 \sim 20$ without $M(K^+K^-)$ requirement, and the signal events are assumed to be distributed uniformly in $M(K^+K^-)^2$ window, which is valid considering the spins of the particles in the decay. Though the increase is not so much, we may use that requirement in the future.
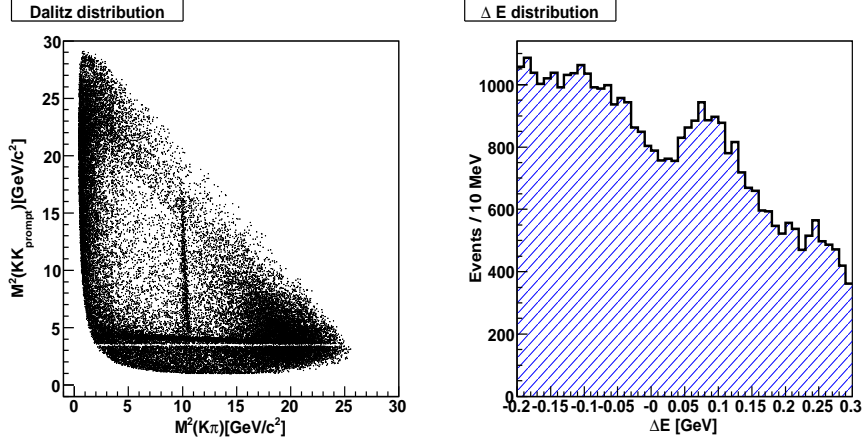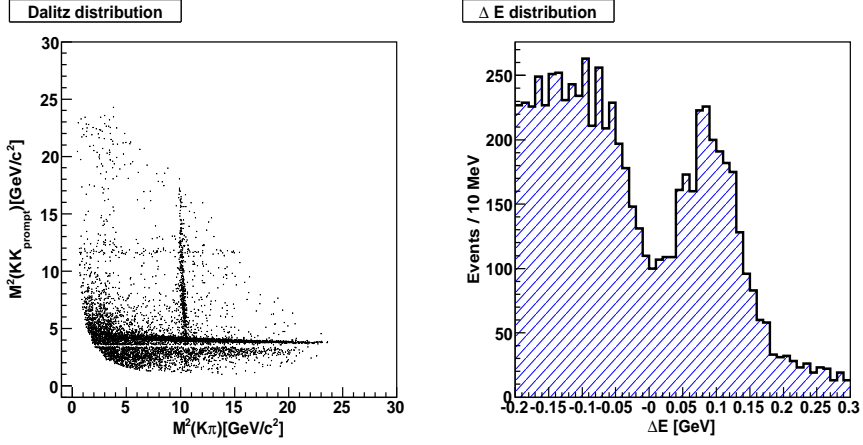

(a) Dalitz and ΔE distributions for the data sample with the $B^- \to D_{\mathrm{sup}}K^-$ selection.
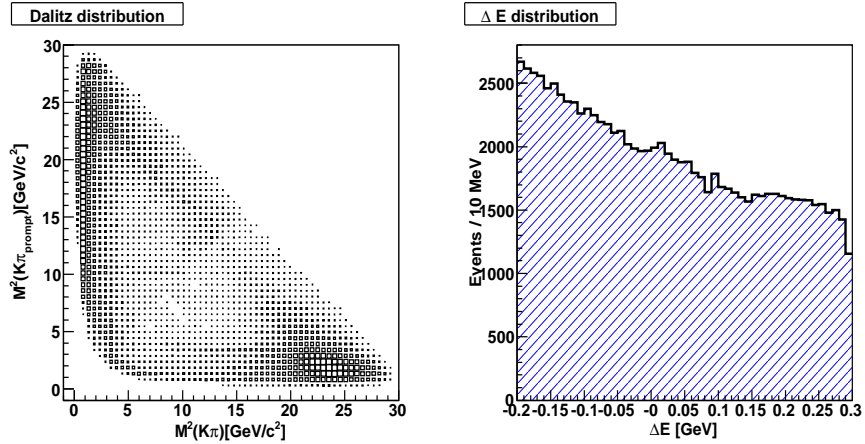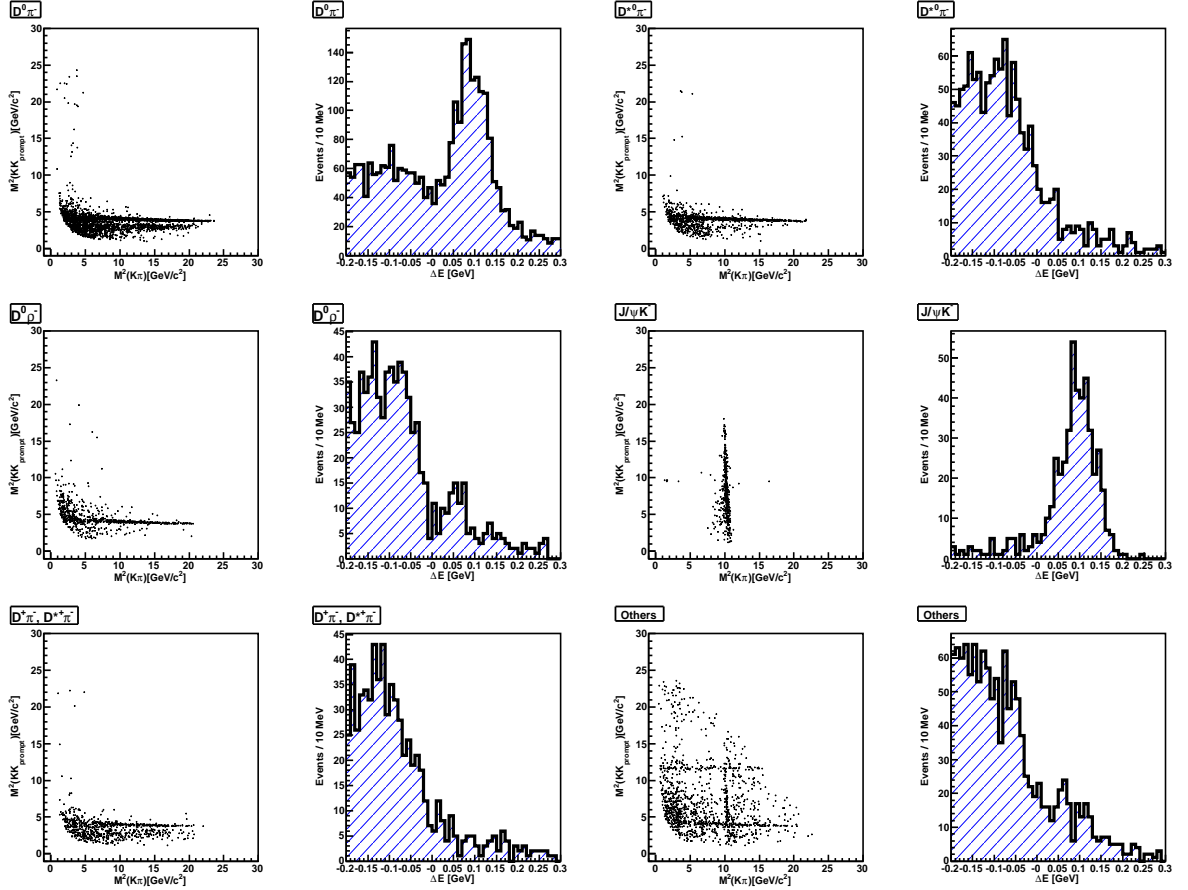

(b) Dalitz and ΔE distributions for the data sample with the $B^- \to D_{\mathrm{sup}}\pi^-$ selection.

Figure A.1: Dalitz and ΔE distributions for the data samples for (a) $B^- \to D_{\mathrm{sup}}K^-$ and (b) $B^- \to D_{\mathrm{sup}}\pi^-$. A lax ΔE cut of -0.2 GeV $< \Delta E < 0.3$ GeV and all the other cuts described in section 4.3 are applied.
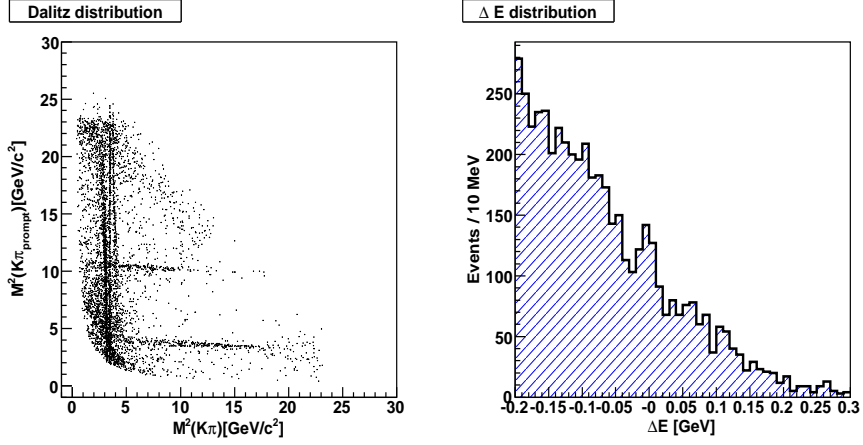
(a) Dalitz and ΔE distributions for $B\bar{B}$ MC samples with the $B^- \to D_{\mathrm{sup}}K^-$ selection.

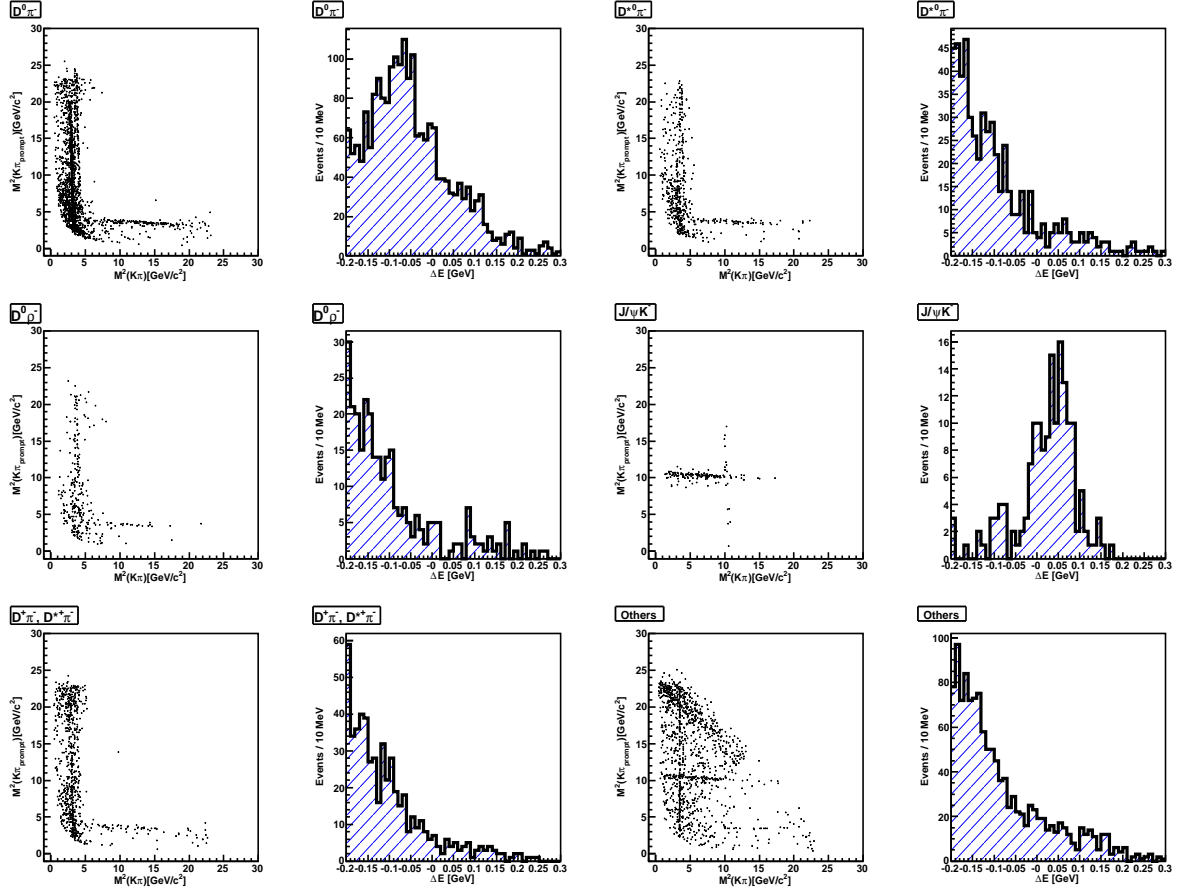(b) Dalitz and ΔE distributions for each components.

Figure A.2: (a) Dalitz and ΔE distributions for the $B\bar{B}$ generic MC samples for $B^- \to D_{\mathrm{sup}}K^-$. A lax ΔE cut of -0.2 GeV $< \Delta E < 0.3$ GeV and all the other cuts described in section 4.3 are applied. (b) Dalitz and ΔE distributions for several decay modes in the $B\bar{B}$ MC sample for $B^- \to D_{\mathrm{sup}}K^-$.

(a) Dalitz and ΔE distributions for $B\bar{B}$ MC samples with the $B \to D_{\mathrm{sup}}\pi$ selection.

(b) Dalitz and ΔE distributions for each components.

Figure A.3: (a) Dalitz and ΔE distributions for the $B\bar{B}$ generic MC samples for $B^- \to D_{\mathrm{sup}}\pi^-$. A lax ΔE cut of -0.2 GeV $< \Delta E < 0.3$ GeV and all the other cuts described in section 4.3 are applied. (b) Dalitz and ΔE distributions for several decay modes in the $B\bar{B}$ MC sample for $B^- \to D_{\mathrm{sup}}\pi^-$.
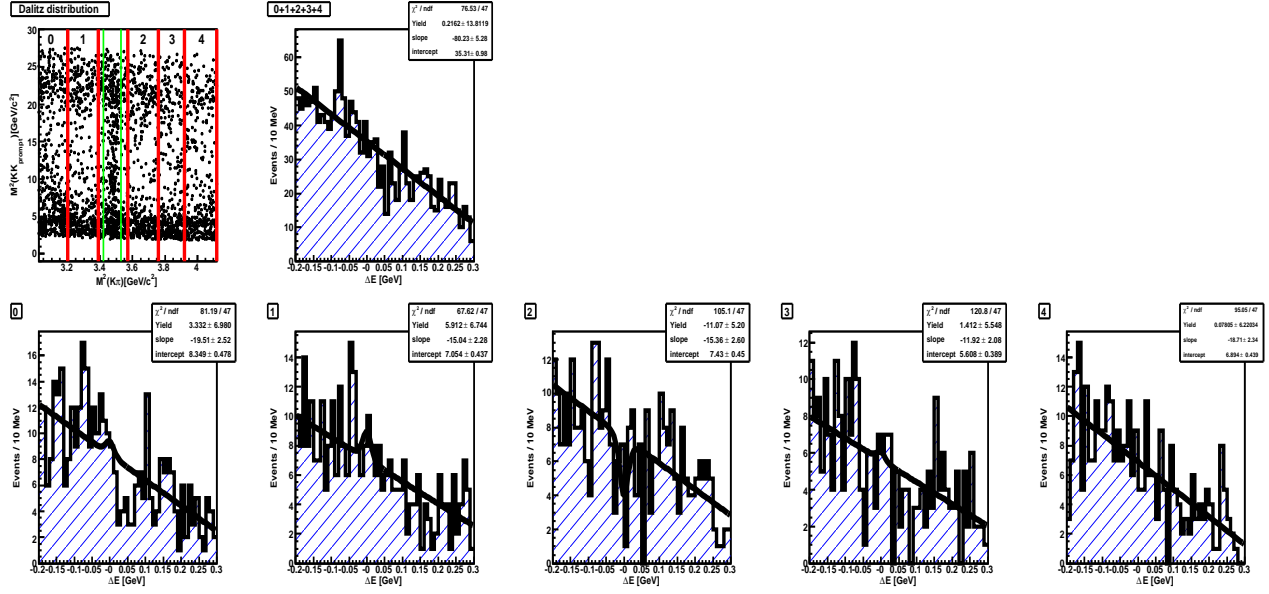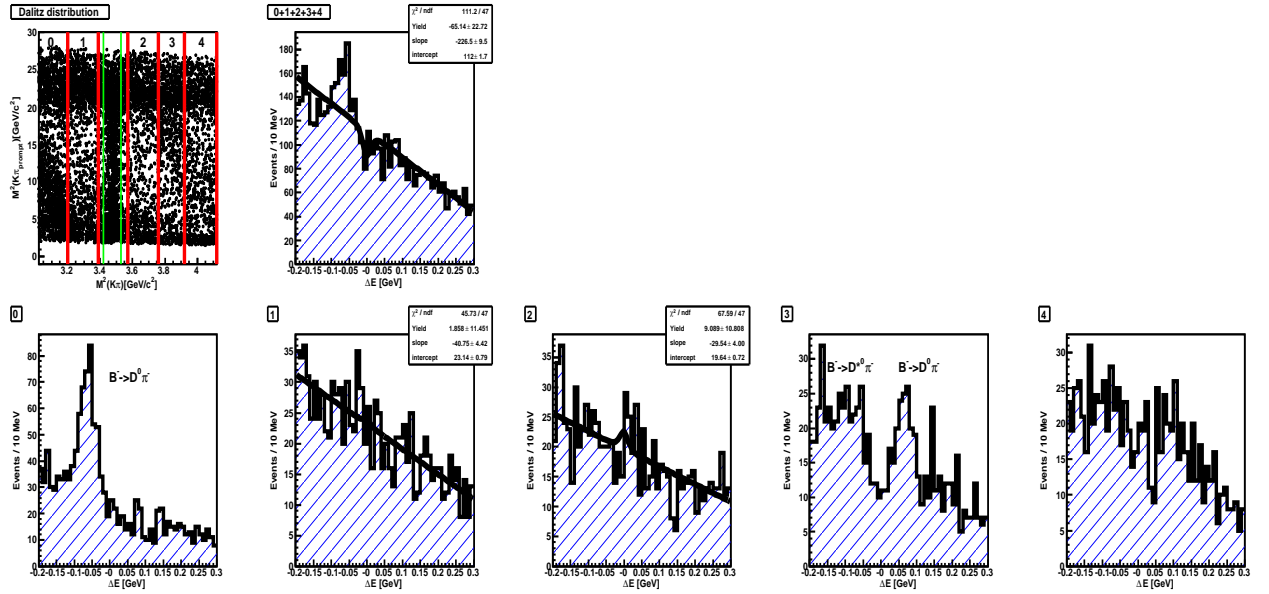
(a) ΔE distributions for some D mass sideband slices of the data sample for $B \to D_{\mathrm{sup}}K$.

(b) ΔE distributions for some D mass sideband slices of the data sample for $B \to D_{\mathrm{sup}}\pi$.

Figure A.4: ΔE distributions for some D mass sideband slices of the data samples for $B^- \to D_{\mathrm{sup}}K^-$ (a) and for $B^- \to D_{\mathrm{sup}}\pi^-$ (b).

Appendix B

Systematic studies

B.1 Systematic study on the particle identification requirement for prompt particle

We check the resulting $B^- \to D^0 h^-$ branching ratio dependence on $P(K/\pi)$ requirement for prompt particle. We have chosen nine selections and the ΔE fits for each selection are shown in the Figure B.1 and B.2. In Figure B.1 no $P(K/\pi)$ requirement is applied and in Figure B.2 $P(K/\pi) \lessgtr$ 0.2, 0.4, 0.6 and 0.8 are used. Pion mass is assigned to track here so that double Gaussian can be used for $B^- \to D_{\text{fav}}\pi^-$ component. For $B^- \to D_{\text{fav}}K^-$, double bifurcated Gaussian is used where the shapes are fixed from $B^- \to D_{\text{fav}}K^-$ signal Monte Carlo with pion mass assigned to the prompt particles; we've gotten nine shapes depending on the $P(K/\pi)$ requirements.

Branching fractions obtained from these fits are shown in Table B.1. We have not calculated the branching ratios for several selections, for which it's difficult to fix ΔE shapes or signal efficiencies. There is small fluctuation for $\mathcal{B}(B^- \to D^0\pi^-)$ so this should be taken as a systematic error. For $\mathcal{B}(B^- \to D^0K^-)$ each values are consistent with each others.

Mode(Condition)	$\epsilon_{D_{\text{fav}}h^-}$ (%)	Yield	$\mathcal{B}(B^- \to D^0h^-)$
$B^- \to D_{\text{fav}}\pi^-(P(K/\pi) < 0.2)$	22.8	27011±180	$(4.75\pm0.03)\times10^{-3}$
$B^- \to D_{\text{fav}}\pi^-(P(K/\pi) < 0.4)$	24.9	29179±187	$(4.69\pm0.03)\times10^{-3}$
$B^- \to D_{\text{fav}}\pi^-(P(K/\pi) < 0.6)$	26.2	30477±190	$(4.66\pm0.03)\times10^{-3}$
$B^- \to D_{\text{fav}}\pi^-(P(K/\pi) < 0.8)$	27.1	31529±194	$(4.66\pm0.03)\times10^{-3}$
$B^- \to D_{\text{fav}}\pi^-(\text{w/o the cut})$	28.4	33040±203	$(4.66\pm0.03)\times10^{-3}$
$B^- \to D_{\text{fav}}K^-(\text{w/o the cut})$	27.9	2374±83	$(3.41\pm0.12)\times10^{-4}$
$B^- \to D_{\text{fav}}K^-(P(K/\pi) > 0.2)$	26.2	2153±60	$(3.29\pm0.09)\times10^{-4}$
$B^- \to D_{\text{fav}}K^-(P(K/\pi) > 0.4)$	25.1	2061±56	$(3.29\pm0.09)\times10^{-4}$
$B^- \to D_{\text{fav}}K^-(P(K/\pi) > 0.6)$	23.7	1945±50	$(3.29\pm0.08)\times10^{-4}$
$B^- \to D_{\text{fav}}K^-(P(K/\pi) > 0.8)$	21.6	1799±49	$(3.34\pm0.09)\times10^{-4}$

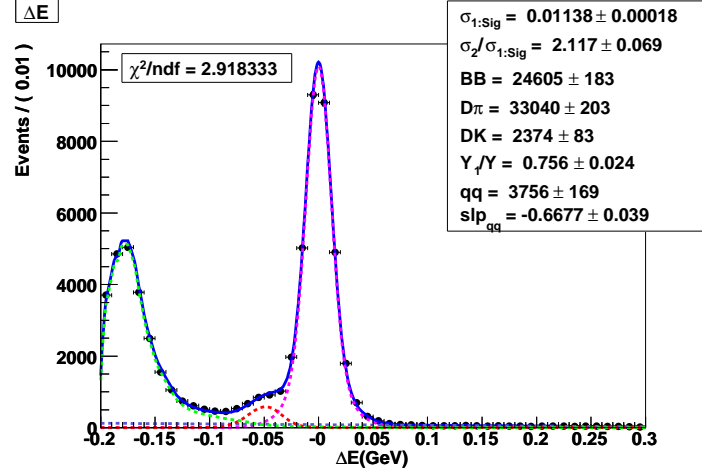Table B.1: Efficiencies, yields and branching ratios are shown.

Figure B.1: ΔE fit for the data without $P(K/\pi)$ requirement for the prompt particles. The mass of pion is assigned for those particles.

B.2   Systematic study on $\mathcal{R}$ requirement

We also check the dependence on $\mathcal{R}$ requirement. ΔE fits and calculated branching ratios are shown in Figure B.3 and Table B.2, where we have applied two requirements, 0.74 and 0.90. We can ignore the systematic error due to the $\mathcal{R}$ requirement.

Mode(Condition)	$\epsilon_{D_{\mathrm{fav}}h^-}$ (%)	Yield	$\mathcal{B}(B^- \to D^0 h^-)$
$B^- \to D_{\mathrm{fav}}\pi^-(\mathcal{R} < 0.74)$	22.8	27236±177	$(4.78\pm0.03)\times10^{-3}$
$B^- \to D_{\mathrm{fav}}\pi^-(\mathcal{R} < 0.90)$	15.7	18747±145	$(4.78\pm0.04)\times10^{-3}$
$B^- \to D_{\mathrm{fav}}K^-(\mathcal{R} < 0.74)$	23.5	1918±52	$(3.27\pm0.09)\times10^{-4}$
$B^- \to D_{\mathrm{fav}}K^-(\mathcal{R} < 0.90)$	15.2	1222±41	$(3.22\pm0.11)\times10^{-4}$

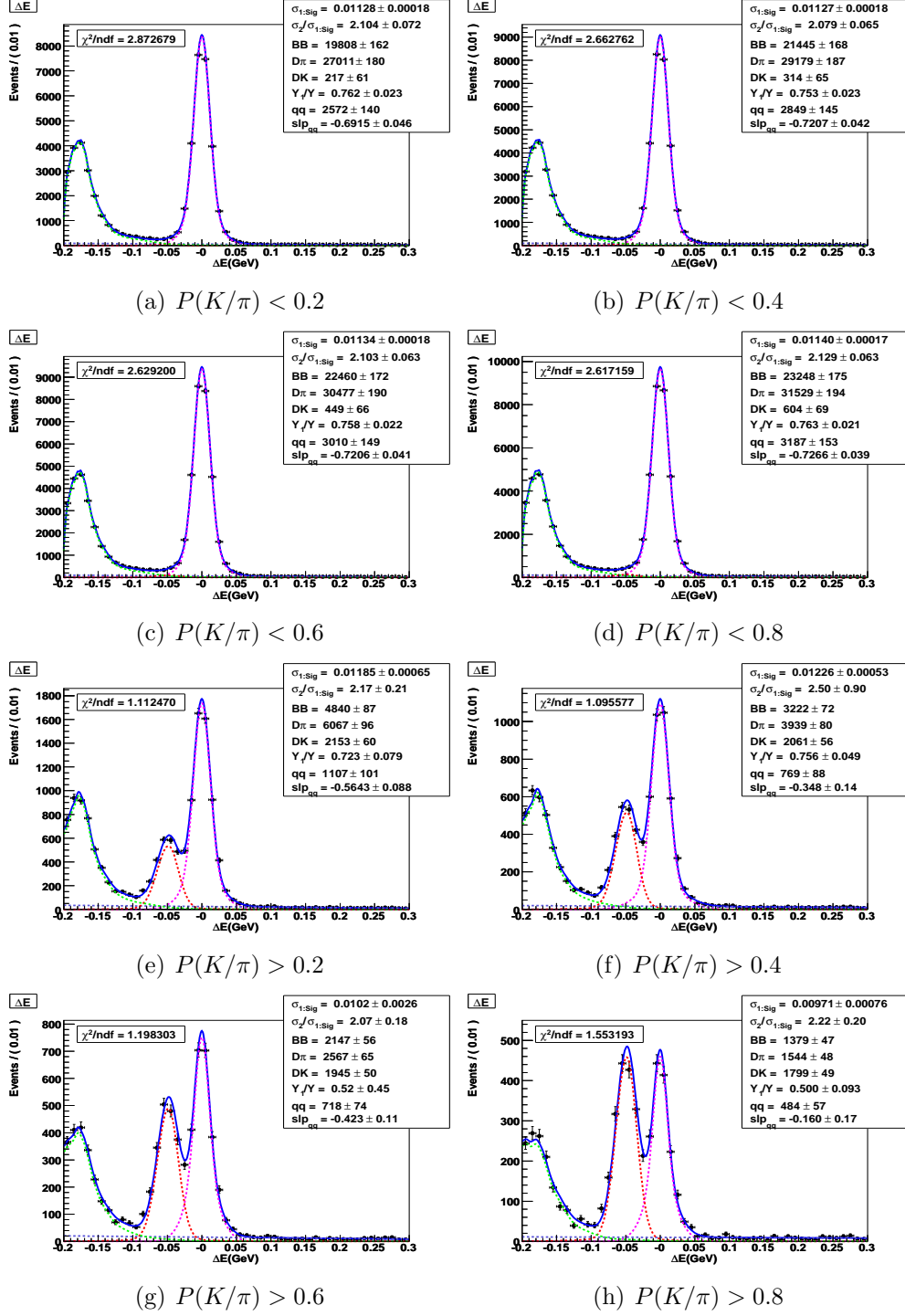Table B.2: Efficiencies, yields and branching ratios for $\mathcal{R}$ dependence check are shown.

Figure B.2: ΔE fits with several $P(K/\pi)$ requirements. We estimate a systematic error from these fit results.
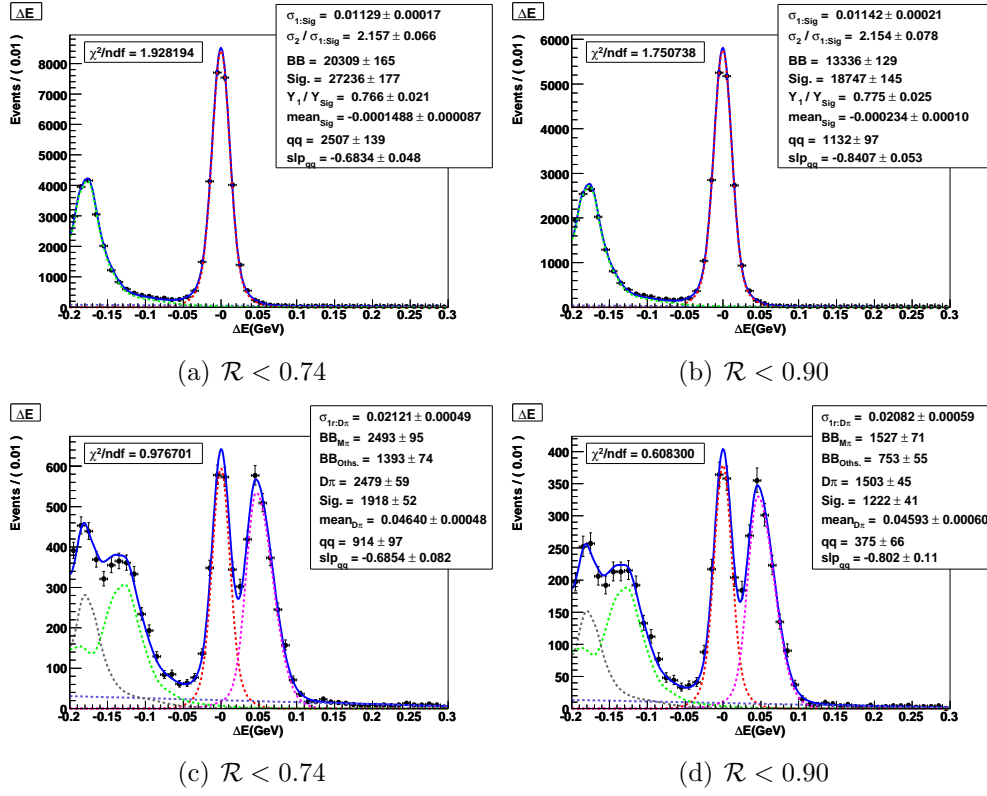
(a) $\mathcal{R} < 0.74$

(b) $\mathcal{R} < 0.90$

(c) $\mathcal{R} < 0.74$

(d) $\mathcal{R} < 0.90$

Figure B.3: ΔE fits with two $\mathcal{R}$ requirements for $B^- \to D_{\text{fav}}\pi^-$ (upper) and $B^- \to D_{\text{fav}}K^-$ (lower).

Bibliography

[1] ILC Global Design Effort and World Wide Study, International Linear Collider Reference Design Report, II-1 (2007).

[2] ILC Global Design Effort and World Wide Study, International Linear Collider Reference Design Report, II-57 (2007).

[3] N. Cabbibo, *Phys. Rev. Lett.* **10**, 531 (1963).

[4] M. Kobayashi and T. Maskawa, *Prog. Theor. Phys.* **49**, 652 (1973).

[5] A. Kusaka, Ph.D. thesis, 11 (2007).

[6] L. Wolfenstein, *Phys. Rev. Lett.* **51**, 1945 (1983).

[7] Particle Data Group, W.-M.Yao *et al.*, 2007 partial update for edition 2008 at http://pdg.lbl.gov.

[8] Y. Grossman *et al.*, *Phys. Rev. D* **72**, 031501 (2005).

[9] A. Amorim *et al.*, *Phys. Rev. D* **59**, 056001 (1999).

[10] M. Gronau and D. London, *Phys. Lett. B* 253, 483 (1991).

[11] M. Gronau and D. Wyler, *Phys. Lett. B* 265, 172 (1991).

[12] D. Atwood, I. Dunietz and A. Soni, *Phys. Rev. Lett.* **78**, 3257 (1997); D. Atwood, I. Dunietz and A. Soni, *Phys. Rev. D* **63**, 036005 (2001).

[13] A. Poluektov *et al.*, *Phys. Rev. D* **70**, 072003 (2004).

[14] A. Giri *et al.*, *Phys. Rev. D* **68**, 054018 (2003).

[15] Belle Collaboration, A. Poluektov *et al.*, *Phys. Rev. D* **73**, 112009 (2006).

[16] BaBar Collaboration, B. Aubert *et al.*, *Phys. Rev. Lett.* **95**, 121802 (2005).

[17] BaBar Collaboration, B. Aubert *et al.*, *Phys. Rev. D* **71**, 112003 (2005); Belle Collaboration, K. Abe *et al.*, *Phys. Rev. Lett.* **93**, 031802 (2004), Belle Collaboration, T. Gershon *et al.*, Phys. Lett. B **624**, 11 (2005).

[18] S. Kurokawa and E. Kikutani, *Nucl. Instrum. Meth. A* **499**, 1 (2003), and other papers included in this volume.

[19] Belle Collaboration, A. Abeshian *et al.*, *Nucl. Instrum. Meth. A* **479**, 117 (2002).

[20] Y. Ushiroda, *Nucl. Instrum. Meth. A* **511**, 6 (2003).

[21] R. A. Fisher, Ann. Eugenics **7**, 179 (1936).

[22] The Fox-Wolfram moments were introduced in G. C. Fox and S. Wolfram, Phys. Rev. Lett. **41**, 1581 (1978). The modified moments used in this analysis are described in Belle Collaboration, S. H. Lee *et al.*, Phys. Rev. Lett. **91**, 261801 (2003).

[23] HFAG, online update for Summer 2007 at
http://www.slac.stanford.edu/xorg/hfag.

[24] Belle Collaboration, Y. Chao *et al.*, Phys. Rev. Lett. **93**, 191802 (2004).

[25] Belle Collaboration, M. Saigo *et al.*, Phys. Rev. Lett. **94**, 091601 (2005).

[26] BaBar Collaboration, B. Aubert *et al.*, Phys. Rev. Lett. **93**, 131804 (2004).

[27] Belle Collaboration, A. Poluektov *et al.*, Phys. Rev. D **73**, 112009 (2006).